Stony Brook University

Thermal Spray Processing of Strain Gauges, Thermocouples and Metal-Ceramic Composite Resistors

A THESIS PRESENTED

BY

EDUARDO JOSE MARI DE L'ISLE

to

The Graduate School
In Partial Fulfillment of the
Requirements
For the Degree of

Master of Science
in
Materials Science and Engineering

Stony Brook University

August 2009

Stony Brook University

The Graduate School

Eduardo Jose Mari Delisle

We the thesis committee for the above candidate for the
Master of Science degree, hereby recommend
Acceptance of this thesis

Prof. Sanjay Sampath – Thesis Advisor
Professor, Materials Science and Engineering Department

Prof. Christopher Weyant
Professor, Materials Science and Engineering Department

Prof. Jon Longtin
Professor, Mechanical Engineering Department

This thesis is accepted by the Graduate School

Lawrence Martin
Dean of the Graduate School

To my wife
For standing next to me
and building her dreams along mine.

… do boldly what you do at all
Fables, Aesop

TABLE OF CONTENTS

List of figures

List of tables

Acknowledgment

I have to thank many, family friends and colleagues for the support, friendship and camaraderie that was there for me when I needed. To all of you thanks.

Special thanks to my advisor Prof. Sanjay Sampath for his wise and opportune advice. I learned from him every time we met, he is always thinking of new and novel ways to push forward the technology, to raise the bar. I learned a new thinking structure. Thank you..

My colleagues at CTSR are also my best friends, they have contributed to me personal growth as much as to my academic development. My special thanks to Yang Tan, Alfredo Valarezo, Kentaro Shinoda, Jose Colmenares, Brian Choi, Gopal Dwivedi, Shanshan Liang, Lorena Bejarano and many more.

Special gratitude to my parents for encouraging me to reach my goals and to never give up.

Funding support from National Science Foundation, MME Program, Grant # 0428708 is acknowledged.

SYNOPSIS

Thermal spray is a material deposition process used for decades to provide thermal, corrosion, and wear protection coatings for engineering components. Powders of the desired coating material are heated in a flame or electric arc to a molten/partially molten state and impinged on a surface where they rapidly cool as ‘splats’ that build to form the coating. Importantly, no adhesive is required between the component and the thermal spray coating. The thermal spray process affords tremendous versatility in the materials that can be deposited, requires no firing or curing of the deposited material, and can readily be used to fabricate multi-layer structures of different materials. Thermal spray has enjoyed a rich history of protecting engineering components in harsh environments, electrical and electronic applications find in thermal spray a fast and cost effective processing method hence the adaptation of this technology for harsh environment sensor applications is a natural one.

Monitoring the conditions of engineering components in high temperature, harsh environments, is of tremendous interest for industrial, commercial, and military applications. Measuring parameters such as temperature, strain, cracks, heat flux, vibration, spallation of coatings, etc. is central to maintaining system reliability as well as providing input for prognosis or condition-based maintenance in which a system is subjected to maintenance based on the actual state of the system, rather than an estimated prediction. Such an approach promises to provide substantially longer lifetimes to engineering systems, while reducing down-time and maintenance costs and minimizing catastrophic failure.

Central to this concept is the ability to measure the desired parameters of interest; however the development of sensors for very harsh environments has remained an elusive challenge. A key challenge is to develop sensor technologies that can be integrated into harsh-environment engineering systems while being cost-effective, easy to implement, have the approval of system designers, and can be repaired in the field.

This thesis addresses the understanding and development of three important classes of sensors produced via thermal spray, an emerging technology for versatile, low cost sensors, they include embedded temperature and heat flux sensors, strain gauges and metal-ceramic resistor composites.

Laser micromachining was used to fabricate strain gauges from sprayed NiCr patches that had different intrinsic residual stresses. Gauges were tested under strain cycling conditions. Electrical resistance drift was observed in both cases as a function of strain. The NiCr patches with the higher residual stress (-144 MPa) exhibited the higher drift. The causes are tracked back to the process parameters and particle state.

Thermal spray processing was used to fabricate thermocouples (TSTC). TSTC were tested to calculate the thermoelectric sensitivity or Seebeck coefficient (S), given that the original powders used differed from nominal composition and that the thermal process induces compositional changes as well. *S* for the TSTC is close to that of type-K thermocouples. TSTC were overcoated with YSZ and tested under high heat flux conditions. The output matches well that of an analytical model for the same system. TSTC proven to be robust and follows closely the system temperature trend.

Finally, two component metal-ceramic resistors were made via HVOF and APS for several metal/ceramic ratios. The composites percolated (electrical percolation) at 6.93 and 5.25 vol%Ni respectively which is much lower than the classical 33% for spheroidal composite systems. The reason for the latter is the anisotropic characteristics of sprayed materials. The experimental results were compared against a previously developed analytical model that correlate flattening ratio to percolation threshold (Pc). The Pc experimental values are higher than the ones predicted by the model. Actual particles splash and fragment upon impact which were not considered in this model. The process-structure for these three sensor systems is presented in the form of topical chapters in this thesis.

Chapter 1 Strain Gauge

Resistive Strain Gauge Sensor Fabrication using Thermal Spray (TS) and Ultrafast Laser Processing: Process Induced Effects on Strain Gauge Response.

1.1 Introduction

1.1.1 Strain gauges

Strain gauges are devices used to measure the strain in a component, commonly made of metallic foil embedded in a polymer that is also used to glue the device to the component. When the component is deformed, the foil is deformed, causing a change in electrical resistance (*R*). *R* is then related to the strain. Strain gauges have widespread use in industrial and commercial applications for instance, engineering components operating in extreme environments or in critical applications where human life could be at risk in case of failure, demand constant monitoring of strain among other factors to ensure operating conditions are under design limits,

Strain gauges are normally designed and fabricated to convert mechanical motions to electronic signals. Two kinds of strain gauges are found in the market, one is resistive and the other capacitive. Since the initial development of strain gauges, there has been a widespread acceptance as they continue to find new and innovative applications.

1.1.1.1 Resistive strain gauges

The most widely used parameter that varies in proportion to strain is electrical resistance. Although capacitance and inductance-based strain gages have been manufactured, the sensitivity of these devices to vibration, mounting requirements, and circuit complexity has limited their application. The ideal

resistive strain gage would change resistance only due to the deformation of the surface to which the device is attached. However, in real applications, temperature, gauge material properties, characteristics of the adhesive that bonds the gage to the surface (bonded strain gauges), all affect the detected *R*.

A typical resistive strain gauge consists of a metal foil mounted on a polymer resin backing film; Figure 1-1 shows the typical pattern of a resistive strain gauge. Metal sensor-elements are dominated by geometric terms; therefore they are relatively temperature independent. Resistive strain gauges are widely used because they are small, cheap, sensitive and reliable. Especially at high temperature conditions, it is almost impossible to find neither a resistant alloys nor bonding agents having stable and repeatable resistance-temperature characteristic to meet the static and quasi-static requirements. Typical polymer based strain gauges usually can't withstand temperatures above 400 °C. This motivates the development of strain gauges that could be applied at high temperatures.

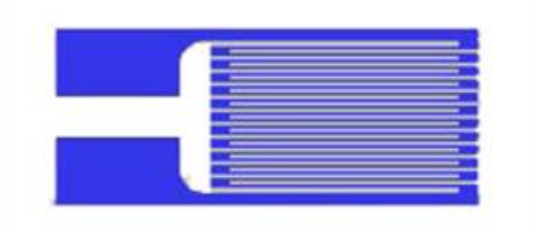

Figure 1-1 Typical pattern resistive strain gauge [1]

When selecting a strain gage, one must consider not only the strain characteristics of the sensor, but also its stability and temperature sensitivity. Unfortunately, the most desirable strain gage materials are also sensitive to temperature variations and tend to change resistance as they age. For tests of short duration, this may not be a serious concern, but for continuous industrial measurement, one must include temperature and drift compensation.

1.1.2 Thermal sprayed (TS) strain gauges

One of the exciting prospects thermal spray technology offers is the fabrication of integrated embedded sensors directly onto components. The idea is that one or many sensors could be integrated into a traditional thermal spray coating to produce what Fasching called “smart” components [2].

Some advantages of thermal sprayed embedded strain gages are[3]:

- Adhesive free, applied directly on component
- High temperature capability
- Low profile – via thin coating
- Conformal and 3D applicability

Commercial strain gauges have a standard resistance of 120 ohms, therefore the geometrical design of the TS strain gauges needs to be tailored to achieve this value. Coatings resistivity varies slightly with the process conditions (Table 1-1), to compensate for this effect one could change the geometry of the TS strain gauge for instance by slightly varying the finger width or length.

Table 1-1 Range of resistivity values for NiCr coatings sprayed at different conditions [4].

Property	Units	Prop/bilk Prop	Property measurements +/- SD		Property range (max-min)/bulk	SD Range (Aver SD/Bulk)
			cond. A	cond. B		
Electrical Resistivity	μΩ*m	1.28-1.36	1.47 ± 0.05	1.38 ± 0.02	8.3	4.4

Thermal spray paired with ultrafast laser micromachining (a subtractive process in which an amplified ultrafast laser is used to remove portions of a continuous solid) to form strain sensors. The ability to deposit a coating and to laser micromachine a strain gauge on it in virtually any surface, opens the possibility for the use of TS strain gauges in conformal components that operate at high temperatures and/or harsh environments since no bonding agent is needed.

1.1.3 Process induced effects in TS gauges

Due to the large number of complexities and stochastic events during the deposition of thermal spray coatings, the following issues exist [5].

-Layer complexity

-Residual stress

-Interlamella and intersplat oxides

-TS gauges are non bulk solids, therefore behave different.

TS strain gauges don't behave in the same way as foil metallic ones made from a continuous (bulk) solid. Residual stress in coatings can be directly related to mechanical properties e.g., hardness, fracture toughness, adhesion, fatigue life, etc [6]. The rearrangement of the microstructure or microcracking along the splat-splat interfaces in the coating due to annealing or strain can lead to a change in the stress state. As a consequence a change in the electrical resistivity [7].

Additionally, monitoring of the deposit build-up and evolution of stresses during spraying, the later achieved via in-situ curvature sensing[8] is fundamental. Combination of these two complementary sensing devices will enable the development of a complete process picture and coating design strategies. Variables such as surface roughness, deposition rates, and deposition temperature as well as particle states can be correlated to stress in real-time describing qualitatively adhesion, cohesion, peening, and microcracking, among other deposition phenomena.

Gauge factor, drift and non linearity are some of the important properties that have to be studied and determined in order to better understand the thermal sprayed strain gauges functionality and applicability[3].

There is a need for a process science approach to link the process control to the applications by means of possible understanding of the particle state,

deposition conditions and properties of the coatings and their integration. Process diagnostics systems and in situ monitoring tools will enable the parameterization of the actual process operation by particle state and stress build-up indicators.

1.1.3.1 Intrinsic stresses in thermal sprayed materials

It's well known that residual stresses develop in the coating and coating-substrate system during thermal spray. It has been accepted that residual stress and other stresses (deposition and thermal) that act during the deposition process, affect the mechanical properties of the system[4, 6, 8, 9] e.g. fracture toughness, elastic modulus, adhesion, micro- and macro-cracking, etc.

The large thermal mismatch and rapid solidification as well as the plastic deformation produced by the particles upon impact generates high magnitude of stresses that cause micro-cracking of brittle materials and creep or yielding in elastic-plastic solids. In the same order of ideas, the origin of stresses can be more specifically related to: i) the net volume change during solidification of the molten droplet, when in good contact with a colder substrate results in large tensile stresses also known as *quenching stress* [10]. ii) when spraying of high kinetic energy particles such as denser semi-molten ones, the plastic deformation generated on the surroundings of the impact zone creates compressive stresses also called *peening stress* [11] that produce strain hardening in plastic materials. iii) when coating and substrate have different coefficient of thermal expansion (CTE), the cooling from the spraying temperature to room temperature generates what is called *thermal mismatch* and creates tensile or compressive stresses on the coating depending on the CTE of the materials involved.

1.1.3.2 Intrinsic stresses in TS strain gauges

In addition to the stress due to strain of the part being monitored, TS strain gauges have to deal with intrinsic stresses from the deposition process e.g.

deposition stress, residual stress, thermal stress [4, 9-11]. Therefore the state of stresses of the coating might be the key to the performance of the sensor. It is possible to tailor the stresses in the coating by controlling the spray parameters, substrate temperature and deposition rate [4].

Operation principle of strain gauges is based on the electrical resistance offered by the device. Since in many cases TS strain gauges will have some degree of residual stress, a non linear relation of the response may exist when the gauge is subject to tension or compression. Therefore, it is important to understand the effect of intrinsic stresses on the gauge performance.

1.1.3.3 Approach to understand the effect of coating residual stress on the strain gauge

Process maps as well as in-situ curvature sensing using the In-Situ Curvature Sensor (ICP) have proven to be an outstanding technique combination to understand and improve coatings [4]. In this study, particle state (by process maps) and residual stress in the coating will be the parameters to define as per to evaluate their effect on the strain gauge.

A Process Map in thermal spray can be described as a series of systematic relationships connecting the process variables to the energetic particle state (kinetic, thermal), the dynamic formation of coatings, their properties and the actual performance [12]. Figure 1-2 presents a first order process map where one process variable in this case the fuel to oxygen ratio rules the particle state. A process maps can also be linked to coating properties, e.g., porosity, modulus, performance, in such cases they are called second order process maps.

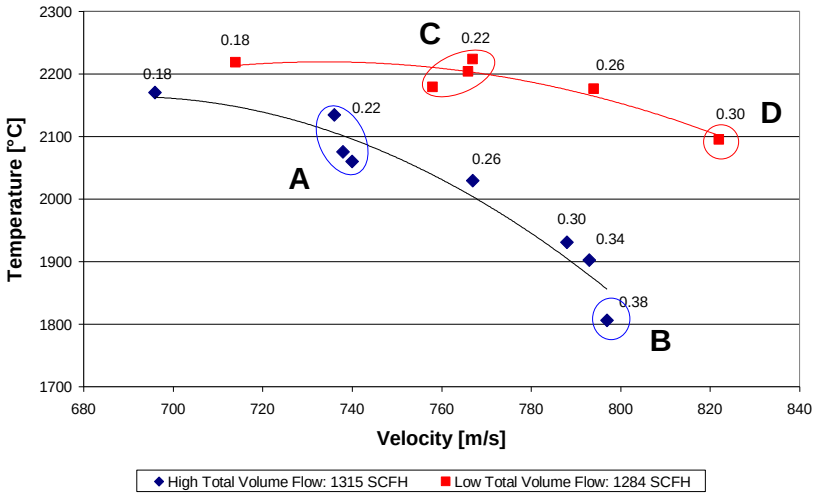

Figure 1-2: Process map for Ni-20Cr using a DJ2700 torch [4].

Of particular interest in the present study are, conditions that display significant difference in coating residual stress which depends on a series of process variables and material selection for example, particle temperature and velocity and coefficient of thermal expansion of the coating and the substrate. The residual stress can be calculated using the final curvature of the sprayed beam (coating + substrate) obtained from the ICP sensor [8]. Other important parameters are the evolving stress during deposition which can be visualized as the difference in slope (curvature over time) of the beam during the coating buildup. The abovementioned can be appreciated in Figure 1-3 for Ni-20%Cr sprayed using DJ2700 torch, and is explained with more detail in the work by Valarezo [4].

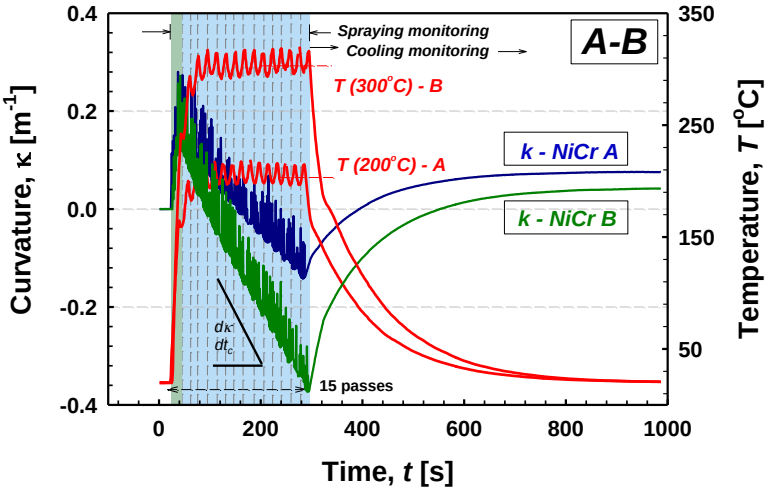

Figure 1-3 Curvature-Temperature evolution of two spraying conditions (A, B) of Ni-20%Cr with DJ2700 torch. Details of these conditions are published in [4].

1.1.4 Objective

Process conditions control to great extend the coating microstructure, e.g., splat characteristics, oxide content, porosity, number of interfaces, interlamella bonding and bonding strength, residual stress among others. Commonly used materials for strain gauges suffer from several issues when exposed to high temperatures, e.g. zero shift, change in electrical resistance of the material (drift), oxidation among others[3]. Therefore to be able to implement these devices in a reliable way at high temperatures, harsh environments, it is necessary to overcome or compensate for those issues. Drift due to mechanical shakedown which is defined herein as the relieve of the coating intrinsic stresses due to microcracking along the splat-splat interface and the relieve of stresses due to annealing at high temperatures, needs to be understood and controlled in order to make strain gauges that can be used for measurements at high temperature.

It is the purpose of this investigation to understand the process induced effects on thermal sprayed strain gauges: Intrinsic residual stresses on the

coating and its effect on the resistance/resistivity change by cyclic strain of the component. Will be investigated by:

- Use process parameters to deliberately modify evolving and residual stress in the coating deposit.
- Study the effect of laser micromachining on TS gauge functionality
- Study the effect of evolving and residual stress on TS strain gauge when subject to cyclic strain.

1.2 Experimental Procedure

1.2.1 Specimen preparation

Strain gauges were fabricated from layered blanket coatings starting with an HVOF thermal sprayed insulating coating of alumina (Al-1110HP Praxair Surface Technologies, Indianapolis, IN) on both sides of a 3.2 mm thick aluminum (Al-6061-T6) cantilever substrate (CS) shown schematically in Figure 1-4. Spraying on both sides of the CS compensates for the remaining curvature otherwise found in the sprayed substrate. Patches of Ni-20%Cr (Ni-105-2 Praxair Surface Technologies, Indianapolis, IN) of 5 x 4 mm where deposited by HVOF process on top of the alumina layer in the configuration shown in Figure 1-4. A water cooled HV2000 torch (Praxair-Tafa, VT, USA), was used to spray the alumina and a water cooled HVOF DJ2700 torch (Sulzer-Metco, Westbury, NY, USA), was used to spray the NiCr. Two different process conditions were chosen to spray the NiCr patches, the process induced effects on the coating from these conditions are very characteristic and dissimilar. One of them produces a coating with higher residual stress than the other [4]. Complete description of the feedstock powders, HVOF torches and process parameters used as well as the value of residual stress in the coating obtained in-situ (as described earlier) can be found in Table 1-2 and Table 1-3.

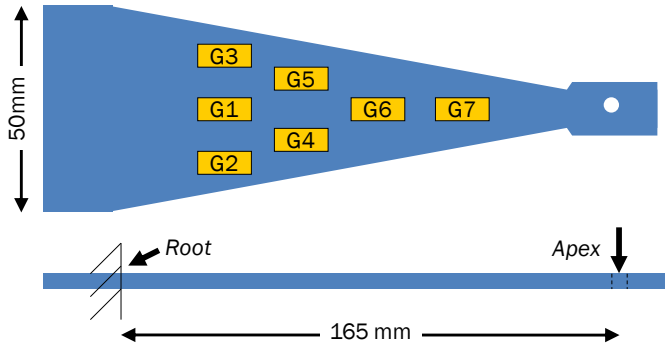

Figure 1-4 Schematic configuration of the cantilever sample with the location of the strain gauges

Table 1-2 Feedstock powders

Material	Production Method	Nominal Composition	Size Range	Morphology
Praxair Ni-105-2	Atomized	Ni-20Cr	-45/+5 μm	Spheroidal
Praxair Al-1110HP	Sintered	99.3% Al_2O_3	-22/+5 μm	Irregular

Coating residual stresses were calculated in-situ utilizing the ICP (Center for Thermal Spray Research, Stony Brook University, stony Brook, NY, USA) which is based on the composite beam theory [13] applied by Matejicek et. al. [8].

Table 1-3 HVOF NiCr Process Conditions

Torch	Condition	Gas Flows					Coating Residual Stress
		Fuel	Oxygen	Air	Carrier	Fuel/oxygen ratio	
		SCFH	SCFH	SCFH	SCFH		MPa
DJ2700	A	128	419	744	50	0.22	-71
	B	163	383	744	50	0.3	-144
HV2000	-	165	600	-	50	0.28	-

Gas Pressures (DJ2700): Fuel (propylene) 110 psi, Oxygen 160 psi, Carrier (hydrogen) 140 psi. Spray distance 266 mm. Traverse torch velocity 0.75 m/s. Feed rate 10 g/min
Gas Pressures (HV2000): Fuel (propylene) 100 psi, Oxygen 150 psi, Carrier (hydrogen) 100 psi. Spray distance 152 mm. Traverse torch velocity 0.75 m/s. Feed rate 15 g/min

1.2.2 Ultrafast Lasers

Ultrafast laser ablation (especially femtosecond lasers) has interesting characteristics for micromachining, notably non-thermal interaction with materials, high peak intensity, precision and flexibility. Ultrafast laser machining is a non-contact process without mask technique. Due to the very short laser pulse duration (150 fs), the laser intensity of laser pulse with 1 mJ is high enough to ablate almost any kind of material with negligible heat affected zone. Another important characteristic of ultrafast laser machining technique is that the fabricated feature size can be small, around 30-50 μm, which is very suitable for

making highly dense interdigitated capacitor. Thermal spray technology also has strong materials versatility. The fact that thermal spray technology can provide multilayer structure with high quality function presents a way to apply for the fabricated sensors working in a hostile environment. For example, a thin ceramic film layer on topic of metal film may work as a protected coating for gauge sensor in harsh environment.

Two ultrafast laser systems are used in this work, the first one consists of a commercial femtosecond laser, the system has four components: i) a femtosecond oscillator (MaiTai, Spectra Physics), ii) an Nd: YLF solid-state pump laser, iii) a Ti: sapphire regenerative amplifier (TR-12A, Photonics Industries) and iv) a 3D precision motorized positioning stage.

The sample is mounted on a 3-D motorized stage. With a resolution of 0.5 μm on each axis over a 50 mm range. The maximum stage velocity is 100 mm/s. A controller connected to a computer software (Labview) is used to create different machining path patterns. TS strain gauges G1, G2, G3 were micromachined using the femtosecond laser.

The second ultrafast laser system used in this study consist of a commercial Ti:sapphire Picosecond Laser coupled with a galvanometer motion system that allows precision cutting of intricate patterns at very high speeds (up to 2500 mm/s) therefore reducing the heat affected zone when cutting metals. Micromachining of the strain gauges with this laser was contracted to an external company. TS strain gauges G4, G5, G6 were micromachined using the picoseconds laser.

1.2.3 Strain Gauge: Geometrical design considerations

The principle of resistive strain gauges has been described above: The change in electrical resistance due to strain is partly due to the geometrical changes taking place in the deformed body and partly due to physical changes

within the metal itself. When the strain gauge is elongated or compressed the geometry of the fingers will change so will the resistance [14]. Therefore the gauge pattern and geometric parameters such as finger length, finger width, finger number and thickness are of great importance. Some of the attributes are: i) Finger Length, when deformation is applied to a strain gauge, the strain will distribute axially from the clamping position to the edge of strain gauge where the force is applied. The strain along the cross direction of strain gauge is assumed to be the same, so this will induce that longer and narrower gauge will have better stress distribution. ii) Finger Width, there is no technical requirement for the finger width of the strain gauges fabricated by ultrafast laser system. Only the gap width between fingers has to be big enough for the laser beam to make a clean cut to the desired depth. iii) Finger Number, the number of fingers is also an important parameter, as the finger number increase, the total length of the conductor increases and therefore the resistance of the strain gauge will increase. iv) Finger thickness, this parameter combined with the finger width provides the cross section area of the conductor, the larger the cross section area of the conductor the smaller the electrical resistance and vice versa.

1.2.4 Cyclic strain test

Strain gauges performance was evaluated in tension and compression at room temperature to evaluate the accuracy of the strain measurements to the actual strain applied. A schematic of the testing rig to be used is presented in Figure 1-5

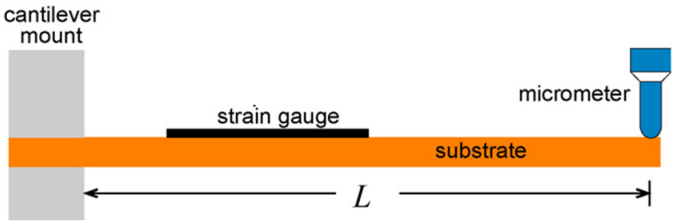

Figure 1-5 Test rig

Samples were tested at +/- 0.350 inches deflection (at the apex of the cantilever sample) for 2500 cycles at a frequency of 1 Hz and the resistance was measured at maximum, minimum and neutral deflections. Samples were tested in a humidity chamber at a temperature of 30 °C and 50% relative humidity. Commercial film strain gauges (CEA-13-240UZ-120) were also positioned next to the thermal sprayed strain gauges and glued using M-Bond2-00 adhesive (Omega Corporation).

For the system used, the strain is calculated as follows:

$$\varepsilon = \frac{w(L)t}{L^2} \qquad \text{Equation 1-1}$$

Where *w(L)* is the applied displacement at the apex, *t* is the thickness of the substrate and *L* is the length from root to apex.

1.3 Results and Discussion

1.3.1 Process induced effects on strain gauge performance

Coating residual stress

Plots of particles temperature vs. velocity and curvature vs. time for conditions A and B are presented in Figure 1-6. Condition B reached higher deposition (surface) temperature than condition A even though the particle temperature was lower. This can be explained by the length of the torch flame which increases with higher fuel ratios. Differences in the microstructural characteristics are observed at different process conditions (Figure 1-7); additionally the higher substrate temperature induces higher tensile stresses due to thermal contraction and the system mismatch in coefficient of thermal expansion [4].

Higher velocity particles will create more peening thus higher compressive stresses; this effect is seen as higher slope in the curvature-time plot [4].

Elastic shake-down has been defined in continuum mechanics as behavior in which plastic deformation takes place during running in, while due to residual stresses or strain hardening the steady state is perfectly elastic [15]. In coatings a similar effect occurs where the electrical resistance drift under the effect of an applied strain due to microcracking and other structural re-arrangements.

In this study process parameters that produce large differences in coating residual stress were chosen. Figure 1-6 shows the process map with the two conditions chosen as well as the curvature-time plots from where the evolving and residual stresses are calculated. The coatings A and B used to make the strain gauges have values of residual stress of: -71 MPa and -144 MPa respectively.

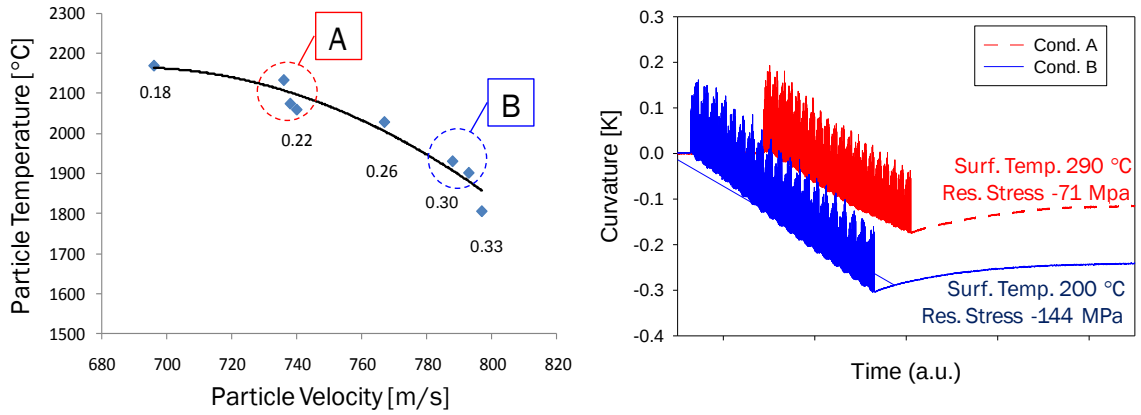

Figure 1-6 Left, Temperature and velocities for conditions A and B used. Right, Curvature

The stresses in the coating-system (substrate+coating) at the end of deposition and cooling are compressive in both conditions which is seen as a negative curvature in Figure 1-6 as defined by the theory of composite beams and further applied by Matejicek [8].

1.3.2 Microstructural evaluation

Figure 1-7 shows the cross-sectional microstructure of the coatings produced with conditions A and B. the coatings exhibit high density and no apparent porosity. Oxide distribution in the microstructure is observed along the intersplat boundaries as well as in the intersplat region. Differences are observed between condition A and B.

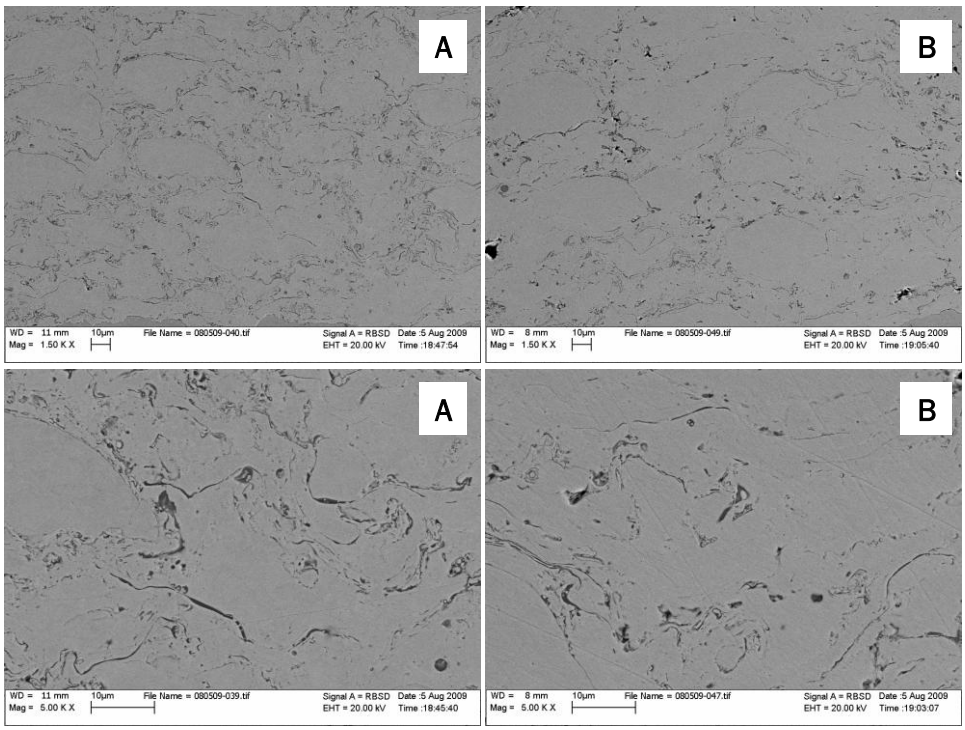

Figure 1-7 SEM images (1.5K x) of Ni-20Cr coatings sprayed at condition A (left) and condition B (right)

Relatively longer residence time in the flame for particles in condition A resulted in a higher degree of surface oxidation producing a microstructure with greater oxide content as can be appreciated in Figure 1-8. Condition B shows lumpier microstructure characterized by rounder splats which are product of a lower particle temperature upon impact, oxidation is also lower for this condition given the shorter residence time and lower particle temperature.

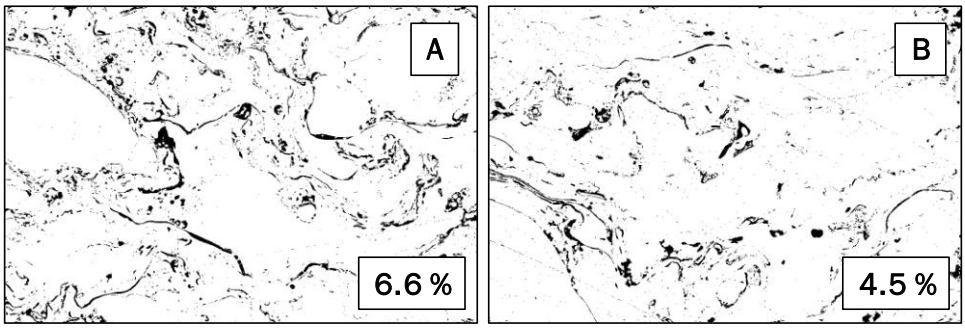

Figure 1-8 Oxide content analysis via image analysis of deposited coatings

It has been reported that NiO and Cr_2O_3 are the main oxides present when producing NiCr coatings via HVOF process [4, 16, 17] in the present study EDAX suggest the presence of Ni and Cr oxides.

1.3.3 Electrical resistance (*R*) change (drift) during strain cycling of TS strain gauges, femtosecond laser micromachined

The TS strain gauges micromachined with the femtosecond laser yielded erratic results as can be appreciated in Figure 1-9 Electrical resistance change of strain gauge G2 (Femtosecond laser micromachined) during strain cycling test.. The effects of non-optimized cutting parameters range from poor gauge performance to complete lack of functionality and its attributed to issues with the optimization of laser parameters such as spot size, pulse duration, non-circular spot geometry and stage displacement speed and step length. Additional results obtained from gauges micromachined with the femtosecond laser are not presented here as substantial additional process improvement is required.

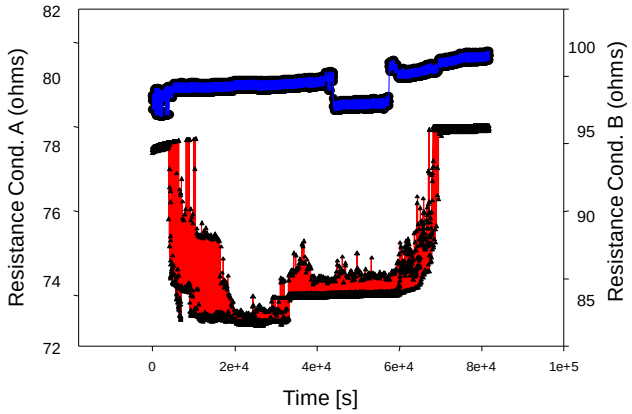

Figure 1-9 Electrical resistance change of strain gauge G2 (Femtosecond laser micromachined) during strain cycling test.

The effect of laser parameters is extended to the quality of the material removal process. Heat affected zone, melting and the subsequent resolidification of the coating are some of the characteristics of poor parameter selection. Laser

micromachining cuts with the two lasers used in this study are presented in Figure 1-10 to Figure 1-13.

Figure 1-10 Show femtosecond laser micromachined lines on NiCr. The material removal is non uniform on the edges of the trench where material is deposited. The continuous and uniform look of the cut suggests local melting and resolidification. Where lines overlap the material removal is accentuated creating a deep hole. 3-D motorized positioning stage limited motion speed can be a factor that influences this results.

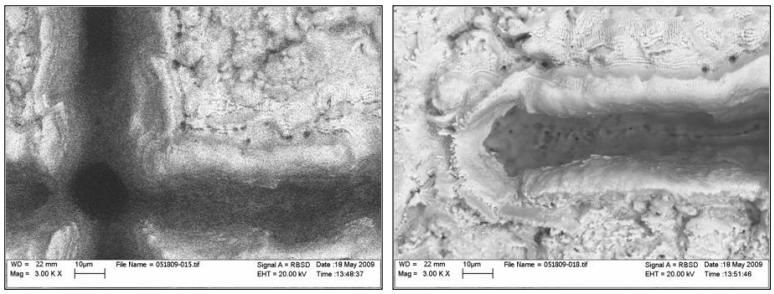

Figure 1-10 Femtosecond laser micromachined lines on NiCr. Left, two lines overlap creating a deep hole. Right, removed material is deposited on the edge of the trench.

The strain gauges are made out of NiCr patches deposited on alumina coated substrates, the goal when removing material is to cut through the NiCr into the alumina without cutting into the substrate. The later would create a thin conductive deposit on the surface that would short the gauge and substrate. Femtosecond laser cuts were made with different processing parameters to evaluate the quality of the cut and optimize the process. Cross section images of the micromachining process different cutting parameters are shown in Figure 1-11 Laser cut on 3 layer system (from the top: NiCr, Alumiina, Steel). Left, various number of passes resulting in cutting into the substrate.. Right, adjusted parameters to remove only the desired layer where the effect of the number of passes was evaluated.

The other laser micromachining system used (picoseconds laser) was contracted to an external company and the parameters where optimized. No reference is available on the parameters used. Figure 1-12 show the laser cuts with this laser system.

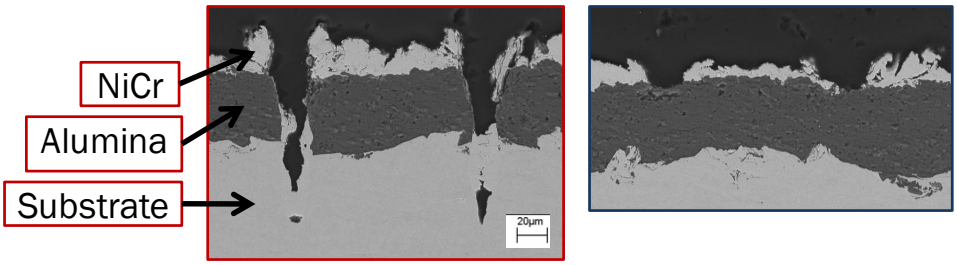

Figure 1-11 Laser cut on 3 layer system (from the top: NiCr, Alumiina, Steel). Left, various number of passes resulting in cutting into the substrate.. Right, adjusted parameters to remove only the desired layer

From the SEM images it can be determined that the spot size used for the micromachining process is in the order of 5µm and several passes are used to remove each layer of every line. It's also observed that the laser cut is done continuously without stopping at the corners neither overlapping at the crossing of two lines. The effect is a very uniform bottom surface. On Figure 1-13 the interface between top and bottom layers is appreciated (NiCr and alumina respectively), no melting or heat affected zone is observed.

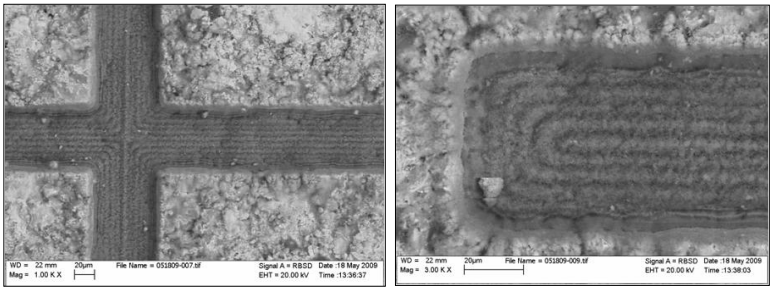

Figure 1-12 SEM image of picosecond laser cut on NiCr

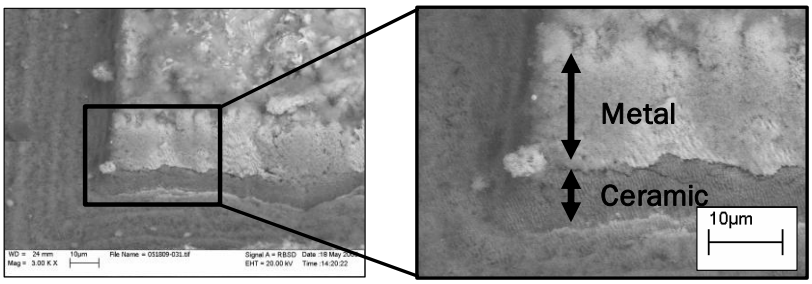

Figure 1-13 SEM image of the interface between NiCr and Alumina on a strain gauge finger, micromachined using a picosecond laser cut.

Figure 1-14 show an actual cantilever sample used for strain testing of the strain gauges (above), 3-D image of two picoseconds laser micromachined strain gauge fingers (bottom). Note that the surface of the fingers is irregular product of the metal deposition process utilized.

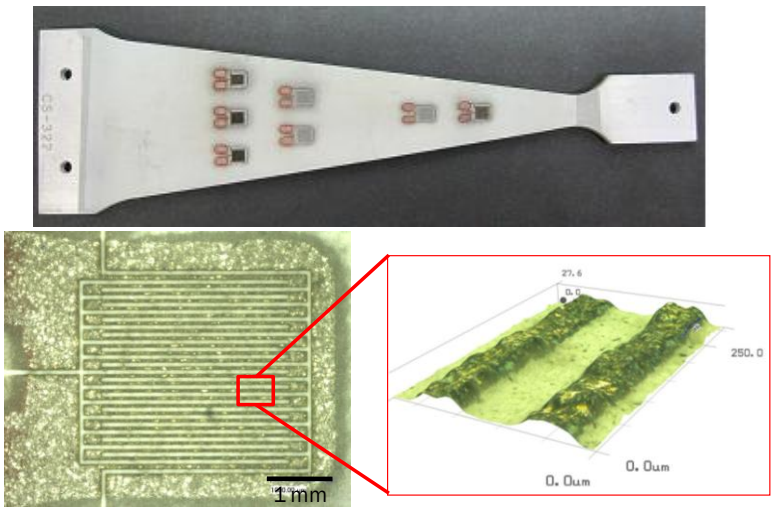

Figure 1-14 Cantilever sample with laser micromachined strain gauges (top), laser cut strain gauge (bottom left), 3D image of the gauge fingers.

1.3.4 Electrical resistance (*R*) change (drift) during strain cycling of TS strain gauges, picosecond laser micromachined

Microcracking along the intersplat boundary during strain cycling could be postulated as a reason for the higher than condition A change in *R*. The fundamental behind that hypothesis is that the higher particle temperature exhibited by condition A induces better intersplat bonding due to better wetting

upon impact [18]. Therefore coatings made with condition A will pose higher fracture toughness than those of condition B. The higher microcracking implies the augmentation of defects hence, the larger increase in electrical resistance of condition B.

It is important to point out that the initial electrical resistance of TS condition B gauges is higher than those of condition A. Assuming geometry does not play a role (same in both cases) then i) variation in electrical resistivity of sprayed coatings can be attributed to oxides, surface roughness, texture and interface adhesion [19]. As shown in Figure 1-8 condition A introduce more of the mentioned defects into the microstructure. However, all coating thicknesses are larger than the electron mean free path for NiCr at room temperature. Hence, the effect on resistivity of the former is minimal or negligible as can be seen on Table 1-1. On another study it is stated that the effect of intersplat oxide content and number of interfaces starts to play affect the electrical resistivity of a coating when elongated, fine elongated interfaces and interlamella oxide and porosity are present like in the case of Triplex (Sulzer Metco) sprayed metals as pointed out by Valarezo [20]. ii) the increase in the atomic net structure defects e.g. dislocations, produced by higher strain hardening of the coating (peening) produced by faster particles impacting on the surface (condition B) has a dominant effect on the electrical resistance.

In average, condition B exhibit 80% more drift after cycling than condition A. in the as sprayed condition, coating B exhibited 102% higher residual stress than condition A.

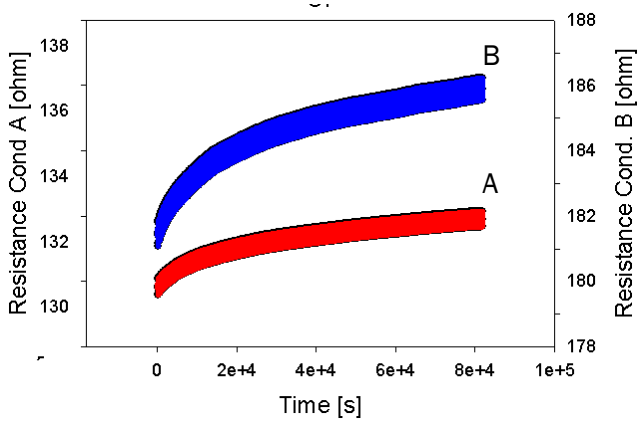

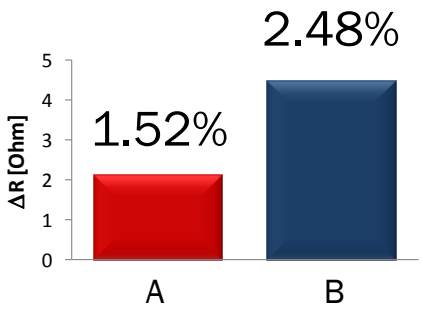

Figure 1-15 Resistance change of strain gauge G4 during strain cycling test (Left), absolute variation in resistance after 2500 strain cycles (Right).

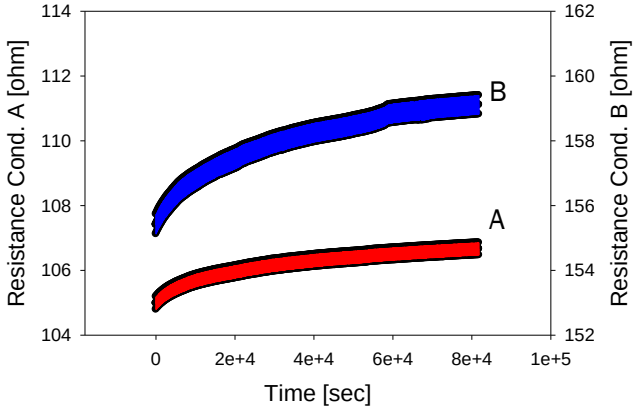

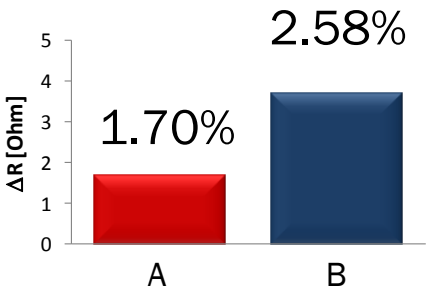

Figure 1-16 Resistance change of strain gauge G5 during strain test (Left), absolute variation in resistance after 2500 strain cycles (Right)

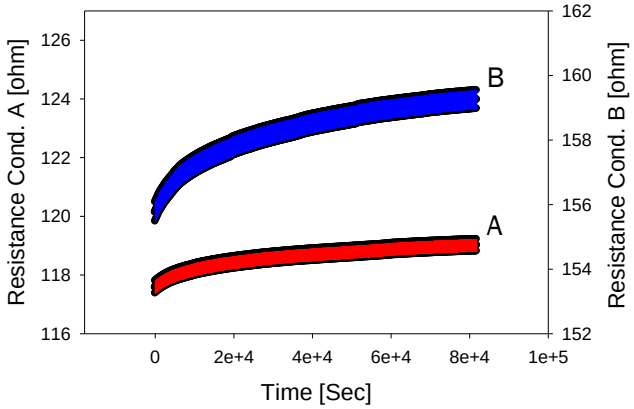

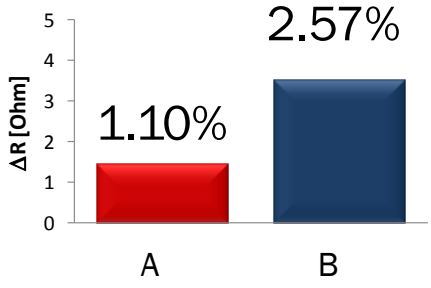

Figure 1-17 Resistance change of strain gauge G6 during strain cycling test (Left), absolute variation in resistance after 2500 strain cycles (Right)

1.4 Summary and Conclusion

The ability to tailor residual stress in the coating and to do it in real time is key to control the properties of the deposit, in this case the change in electrical resistance under cyclic strain of the TS strain gauges.

- Electrical resistance drift from the initial value increases with increase in coating residual stress. This can be linked to process parameters used to deposit the coating.
- Condition B exhibit 80% more drift after cycling than condition A. in the as sprayed condition, coating B exhibited 102% higher residual stress than condition A.
- Femtosecond laser parameters need to be improved to avoid issues like melting and resolidification of laser cut edge and heat affected zone. Therefore improve the functionality of micromachined TS strain gauges
- 3-D motorized positioning stage limits the lasers ability for sample processing.

Chapter 2 Synthesis and Analysis of Embedded Thermocouples in Thermal Barrier Coatings

2.1. Introduction

Higher efficiency and lower costs demand pushes to always increase the limits of operation temperatures in gas turbine engines. However, achieving higher engine operating temperature requires accurate knowledge of the turbine blade temperature for control purpose [21]. Thermal barrier coatings are added to the system to reduce the metal temperature therefore the heat flux during operation. Hence, ceramic TBC's in gas turbine engine components are exposed to harsh environments with ever-increasing operating temperatures and extended service time. Providing accurate assessment of temperature is critical for engineering design and the ability to provide in-situ sensing and health monitoring are essential.

Monitoring these components at high temperature, in extreme environment has been a focal point of interest for commercial and military applications. The ability to monitor temperature and heat flux among other parameters is key to assess system reliability as well as condition-based system prognosis and maintenance based in the actual state of the system, rather than on model estimation. Central to this concept is the ability to measure the desired parameters of interest in very harsh environments, which has remained a challenge, especially considering that the process has to be cost effective and easy to implement

Since the introduction of the concept of "smart coatings" by Fashing [2] who using TS fabricated thermocouples that yielded Seebeck coefficients relatively close to those of commercial devices and were tested up to 200 °C, important advances have been done in thermal sprayed sensors [3, 5, 22-24] as well as alternative non contact technologies for temperature sensing [25-27]. The recent development of direct-write thermal sprayed thermocouples with low-

profile (< 25 μm), conformal and 3D applicability [3, 5] and thermal sprayed strain gauges and thermopiles [5] have opened the door for the implementation of heat flux and other sensors into TBCs. However, stability of the thermocouples at high operation temperatures, zero shift (drift) over time and the intrusive nature of the device remains a challenge for this technology to cross the threshold of research into direct application. In this study thermal sprayed thermocouples are embedded within the layers of a TBC to study its stability, effect on the overall coating and to combine the results with a one dimensional heat flux model to assess the reliability of the reading.

2.2.1 Temperature sensing methodologies

2.2.1.1 Luminescence

One method of determining the temperature of a component without making physical contacts is from measurement of the luminescence decay lifetime of a phosphor either embedded in the component or printed on its surface. This Bradley [26] used a thin sheet of temperature-sensitive phosphor to show distribution of temperature, is particularly attractive in measuring temperature in aggressive environments but has generally been limited to materials that are both stable and exhibit temperature-dependent luminescence decay. However, some of these compounds are neither phase compatible with the oxide formed on superalloys, and their bond-coat alloys, in air at high temperatures nor do they exhibit the low thermal conductivity required for thermal barrier coatings. Gentleman and Clarke [25] used europium doping as a source of strong luminescence as well as characteristic temperature-dependant luminescence lifetimes at high temperatures in pyrochlore zyrconates which are alternative materials to the presently used yttria-stabilized zirconia for thermal barrier coatings. However its feasibility still remains to be proven[28].

2.2.1.2 Pyrometers

Pyrometers have become an important tool in the development of advanced high temperature turbines for use in gas turbine engines. Real time flame discrimination permits accurate operation in the gas turbine environment with high flame content [29]. This versatile capability has been used in a number of ways: i) in experimental engines where a fixed angle pyrometer can be used to monitor for excessive temperature and ii) to measure average blade temperature. This technology however, has many limitations and disadvantages e.g. need for post processing of signal to remove environment effects, reflected radiation can produce errors, deposits on the pyrometer lens and more[21].

2.2.1.3 Thermocouples

Thermocouples are devices based on the thermoelectric effect which is the conversion between temperature differences and electric voltage. Two dissimilar metals produce a voltage proportional to the temperature difference between the junctions due to the Seebeck effect [30]. Many commercial thermocouples types are available and the selection depends usually on the desired range of temperatures, required precision of the output reading, cost among others. Type K thermocouples are affordable, have a high output voltage (Seebeck coefficient) and work over a wide range of temperatures. Type K thermocouples are made using two thermoelectric materials: Chromel (Ni10Cr) and Alumel (Ni2Al2Mn1Si) creating a circuit with positive and negative polarities respectively [30].

The change in material electromotive force (EMF) with respect to temperature is called the Seebeck coefficient or thermoelectric sensitivity. This coefficient is usually a nonlinear function of temperature. Commercial K-type thermocouples typically have a sensitivity of 41.1 $\mu V/^{o}C$.

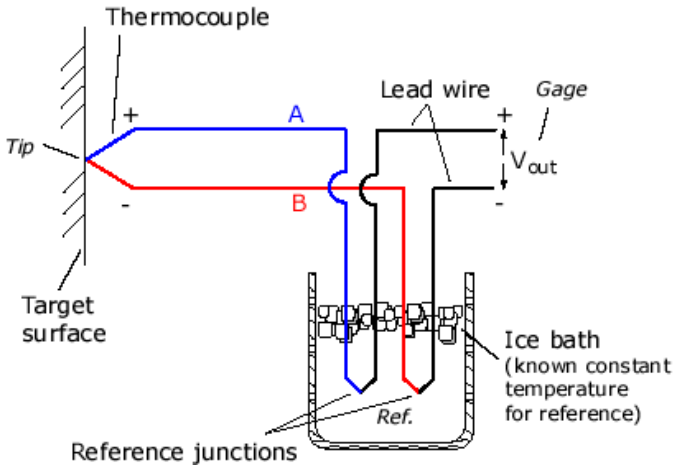

Figure 2-1 Typical Thermocouple Circuit

A thermocouple is a relative temperature sensor but not an absolute one. In other words, a thermocouple requires a reference of known temperature which is provided by ice water in the above illustration (Figure 2-1). Although ice water is easy to obtain and good reference, it's use is not practical and rather inconvenient. Thus, common commercialized thermocouples often includes another temperature sensor, such as thermistor to provide the reading of the reference (room/surrounding) temperature and automatically compensates at the reference junction.

Suppose that the Seebeck coefficients of two dissimilar metallic materials, metal A and metal B, and the lead wires are S_A, S_B, and S_{Lead} respectively. All three Seebeck coefficients are functions of temperature, V_{out} the voltage output measured at the gage, T_{Ref} is the temperature at the reference point, T_{Tip} is the temperature at the probe tip.

If the Seebeck coefficient of the two thermocouple wire materials are pre-calibrated and the reference temperature T_{Ref} is known, the temperature at the probe tip becomes the only unknown and can be directly related to the voltage readout. Then, assuming that the Seebeck coefficients are nearly constant across the targeted temperature range then, the temperature at the probe tip can be expressed as:

$$\boldsymbol{T_{Tip} = T_{Ref} + \frac{V_{out}}{S_A + S_B}} \qquad \textbf{Equation 2-1}$$

2.2.2 Thermal sprayed thermocouples

Fasching et. al., [2] was a pioneer in this technology using thermal spray (TS) to fabricate thermocouples (TSTC) that yielded Seebeck coefficients relatively close to those of commercial devices and were tested up to 200 °C. Recently an improved design for high temperature operation has been developed and tested successfully to over 1000 °C [3] a schematic of the device is shown in Figure 2-2.

The improvements in this field and the reduction in the degree of intrusiveness of recent devices like, for instance the concept of direct write thermocouples [5, 22] which can be applied directly on the component with minimal disturbance of functionality. Another important feature of TSTC is that no bonding substance is necessary between the gauge and the component to monitor.

2.2.3 Embedded thermocouples for heat flux measurement

The integration of sensors in coatings has attracted the imagination of researchers and engineers alike. Many studies have approached sensing surface temperature in high heat flux environments [26, 31-33] but most require expensive, time consuming preparation and controlled atmosphere environments to produce the sensors. Fasching et. al., [2] proposed the production of coatings with embedded sensors via thermal spray such as thermocouple arrays as a way to open up a new dimension for thermal spray technology in what he called “smart coatings”. More recent work on thermal sprayed embedded sensors include thermocouple and embedded thermocouple arrays to create heat flux sensors in ceramic TBC’s [3, 22].

Recent developments in direct write concepts based on thermal spray technology have allowed for incorporating sensors within layers of thermal sprayed thermal barrier coatings. By carefully placing thermocouples within a

ceramic thermal barrier coating (TBC) at different depths, it is possible to extract heat flux through the coating and also examine temperature gradients within the ceramic TBC.

In contrast to measuring temperature, which is a thermodynamic property, heat flux sensors require non-equilibrium conditions in which a temperature difference ΔT is developed across a thermal resistance (*R)* in the presence of a heat flux *q''*. By measuring the temperatures across *R*, the heat flux can be determined according to the following [5]:

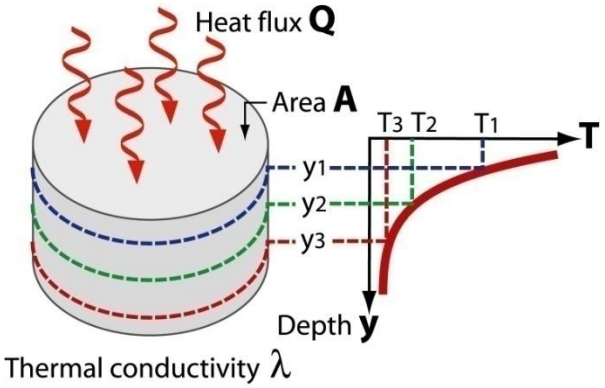

Figure 2-2: Schematic of a multilayer heat flux sensor consisting of three embedded direct-write thermocouples within a TBC [5].

In this device temperature sensors in three different layers are used to determine the heat flux passing through it. It was tested at high temperature using a flame test rig in which an oxyacetylene torch is brought into proximity to the sensor's front side and the temperature readings from the sensors are recorded. Results from such test have been found to be repeatable and consistent. Using an appropriate thermal model, the heat flux can be determined [5].

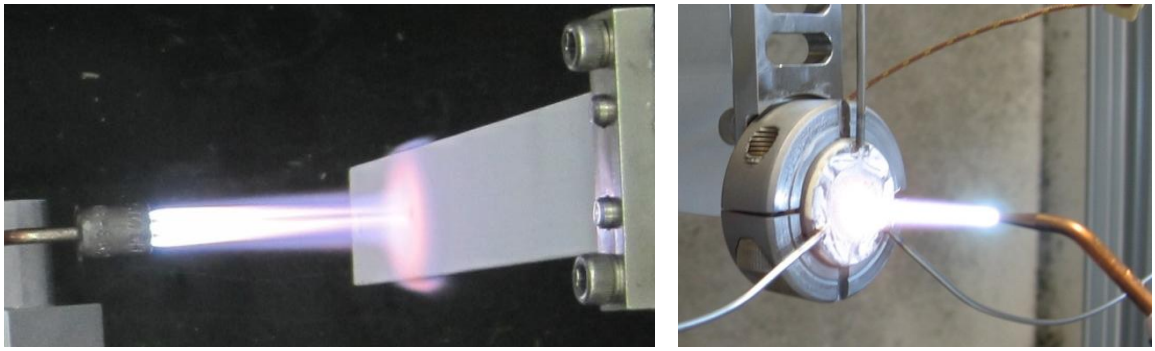

Figure 2-3: Photograph of heat flux sensors embedded in TBC. Burner rig high heat flux test.

2.3 Experimental procedure

2.3.1 Thermal Sprayed Embedded Thermocouple preparation.

Thermal-sprayed K-type thermocouples were fabricated by spraying conductor films of two thermoelectric materials on top of a 229x25.4x1.6 mm Inconel-718 beam that had been previously coated with 0.150 mm of APS sprayed TBC (8YSZ #204 HOSP Saint Gobain, Worcester, MA, USA) using a F4 torch with an 8mm nozzle (Sulzer Metco, Westbury, NY, USA) , a 0.150 mm of a HVOF sprayed bond coat (CoNiCrAlY, CO-240, Praxair Surface Technologies, Indianapolis, IN) using a JetKote torch (Delloro-Stellite, Goshen, IA, USA). The films were sprayed using a hard mask that allowed depositing two thermocouples with a pattern as the one presented in Figure 2-4 using a DJ2700 HVOF torch (Sulzer Metco, Westbury, NY, USA) with propylene as fuel. See Table 2-1 for detailed process parameters. The feedstock used to spray the thermocouple positive conductor film was 80Ni/20Cr (Ni-105-2, Praxair Surface Technologies, Indianapolis, IN) and for the negative conductor film 95Ni/5Al (Diamalloy 4008NS, Sulzer Metco, Westbury, NY). Table 2-3 presents complete information of the feedstock powders used.

Table 2-1: HVOF Process parameters for thermocouple fabrication

Condition	Torch	Gas Flows						Particle State	
		Fuel		Oxygen	Air	Carrier	Fuel/oxy ratio	Temperature (°C)	Velocity (m/s)
		Propylene	Hydrogen						
		SCFH	SCFH	SCFH	SCFH	SCFH			
1	DJ2700	128	-	419	744	50	0.22	2200	737
2		163	-	383	744	50	0.30	2000	780
3	JK	-	1250	440	-	60	2.84	1850	730
Gas Pressures for DJ2700: Fuel (propylene) 110 psi, Oxygen 160 psi, Carrier (hydrogen) 140 psi. Spray distance 266 mm. Traverse torch velocity 0.75 m/s. Feed rate 7 g/min									
Gas Pressures for JK: Fuel (H2) 150 psi, Oxygen 150 psi, Carrier (Argon) 100 psi. Spray distance 229 mm. Traverse torch velocity 1 m/s. Feed rate 32g/min									

Table 2-2 APS process parameters for depositing the TBC

Gas Flows			Energy		Particle State	
Argon	Hydrogen	Carrier (Ar)	Current	Voltage	Temperature	Velocity
SLM	SLM	SLM	A	V	°C	m/s
47.5	6.2	3.5	550	61.6	2842	162
F4 torch, 8mm Nozzle. Traverse torch velocity 0.5 m/s. Feed rate 30 g/min.						

Table 2-3 Feedstock characteristics

Material	Production Method	Nominal Composition	Size Range	Morphology
Praxair Ni-105-2	Atomized	Ni-20Cr	-45/+5 μm	Spheroidal
Sulzer Metco 4008 NS	Gas atomized	Ni-5Al	-45/+10 μm	Spheroidal
Saint Gobain 204	Agglomerated & sintered	ZrO_2-7.5(Y_2O_3)	-70/+10μm	HOSP
Praxair CO-210-24	Atomized	Co-32Ni-21Cr-8Al-0.5Y	-45/+20 μm	Spheroidal

The design of the thermal sprayed thermocouple incorporates one common negative conductor film made with the NiCr and two independent

positive ones made with the NiAl (see Figure 2-4), this approach is intended to minimize the required surface area on the TBC that is occupied by the films.

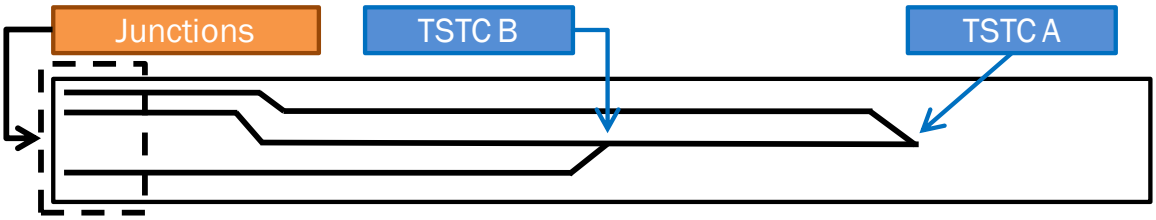

Figure 2-4 Sprayed thermocouples layout. Top two films are the positive contact and bottom one is the negative one.

2.3.2 Thermoelectric Sensitivity (Seebeck coefficient) determination

As explained before, slight changes in composition in the thermoelectric materials generate a change in the Seebeck coefficient of the thermocouple. To measure the TSTC Seebeck, reference type K thermocouples (Ref.TC) (Omega SA1XLK, Omega, Stamford, Connecticut, USA) were bonded next to the tip of the sprayed thermocouples using ceramic putty and introduced in a furnace where temperature was increased in 50 °C steps until the desired temperature and immediately cooled down to avoid possible oxidation or degradation of the films. The test was repeated two times to verify repeatability of the results.

Figure 2-5: Setup to measure the Seebeck coefficient for the sprayed TSTC.

The registered voltages from both thermocouples were plotted against the reference output. The coefficient from a linear fit on the TSTC plot provides the Seebeck coefficient.

2.3.3 Temperature correction due to secondary electromotive force (EMF) generation

The lead or connecting wire should match the TSTC composition closely so as to substantially prevent the generation of thermal EMF at the lead wire junction. In the case of TSTC the thermal process itself induces compositional changes due to oxidation and other phenomena when the powder is passed through the plume [23]. In order to compensate for the EMF generated by the connecting wires, an independent measurement of the temperature is needed at the contact pads located at the root of the sample[23]. For example, the temperatures of the TSTC A and B (Figure 2-6) are determined by measuring the voltages V_A and V_B. The voltages are related to the temperatures by the following equations: [23]:

$$\mathbf{V_A} = \boldsymbol{S_{Kx}}\left(\boldsymbol{T_{tip}} - \boldsymbol{T_{root}}\right) + \boldsymbol{S_K}\left(\boldsymbol{T_{root}} - \boldsymbol{T_{ref}}\right) \quad \text{Equation 2-2}$$

$$\boldsymbol{V_B} = \boldsymbol{S_K}\left(\boldsymbol{T_{root}} - \boldsymbol{T_{ref}}\right) \quad \text{Equation 2-3}$$

Where S_{Kx} is the Seebeck coefficient of the TSTC, S_K is Seebeck coefficient of the type K commercial thermocouple, T_{tip} is the actual temperature at the thermocouple tip, T_{root} is the actual temperature at the root of the sample, T_{ref} is room temperature at the reference contacts.

If the reference contacts are compensated for room temperature by the data acquisition card, the equation becomes:

$$\mathbf{V_A} = \boldsymbol{S_{Kx}}\left(\boldsymbol{T_{tip}} - \boldsymbol{T_{root}}\right) + \boldsymbol{S_K}(\boldsymbol{T_{root}})$$ Equation 2-4

Hence

$$\boldsymbol{V_B} = \boldsymbol{S_K}(\boldsymbol{T_{root}})$$ Equation 2-5

Subtracting equations 3.4 from 3.3 gives:

$$\mathbf{V_A} - \boldsymbol{V_B} = \boldsymbol{S_{Kx}}\left(\boldsymbol{T_{tip}} - \boldsymbol{T_{root}}\right)$$

$$\left(\boldsymbol{T_{tip}} - \boldsymbol{T_{root}}\right) = (\mathbf{V_A} - \boldsymbol{V_B})/\boldsymbol{S_{Kx}}$$ Equation 2-6

Solving equation 2.5 for T_{root} gives:

$$\boldsymbol{T_{root}} = \boldsymbol{V_B}/\boldsymbol{S_K}$$ Equation 2-7

Substituting equation 2.6 into 2.5 gives:

$$\left(\boldsymbol{T_{tip}} - \boldsymbol{V_B}/\boldsymbol{S_K}\right) = (\mathbf{V_A} - \boldsymbol{V_B})/\boldsymbol{S_{Kx}}$$

$$\boldsymbol{T_{tip}} = \frac{(\mathbf{V_A} - \boldsymbol{V_B})}{\boldsymbol{S_{Kx}}} + \frac{\boldsymbol{V_B}}{\boldsymbol{S_K}}$$ Equation 2-8

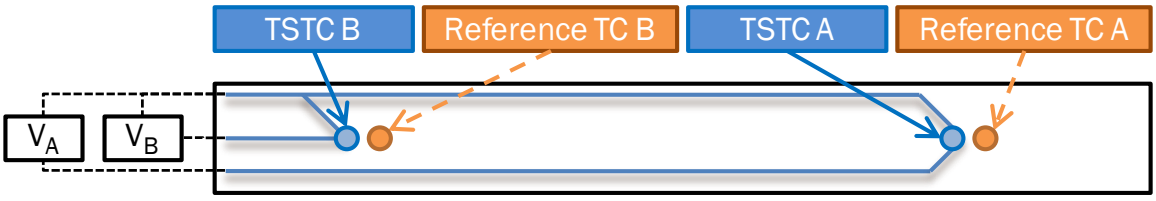

Figure 2-6: TSTC and reference thermocouples layout

2.3.4 One Dimensional Heat Conduction Model. Constructed in collaboration with Y. Tan[1].

The problem of heat transfer in TBCs at normal operating temperatures (>1000 °C) is a very complex one where conduction and radiation compete for a dominant role in the process [34].

[1] Y. Tan is a Post Doctoral Associate at Center for Thermal Spray Research, Stony Brook University, Stony Brook, NY, USA

In TBC systems the heat flux is mainly along the coating through thickness direction, therefore it is valid to model this process with a one dimensional (1-D) approach. In which case and assuming that heat flux is constant and the material has a homogeneous thermal conductivity, the Fourier's law can be applied:

For the TBC $q'' = K_1 \frac{\Delta T_1}{t_1}$ Equation 2-9

For the Substrate $q'' = K_2 \frac{\Delta T_2}{t_2}$ Equation 2-10

For the system $q'' = K_{eff} \frac{\Delta T_1 + \Delta T_2}{t_1 + t_2}$ Equation 2-11

Where q'' is the heat flux, ΔT_1 and ΔT_2 are the temperature difference through the system, t_1 and t_2 are the thicknesses of coating and substrate respectively and K_1, K_2 and K_{eff} are the thermal conductivities of coating, substrate and the system respectively. A schematic of the 1-D model defined is described in Figure 2-7

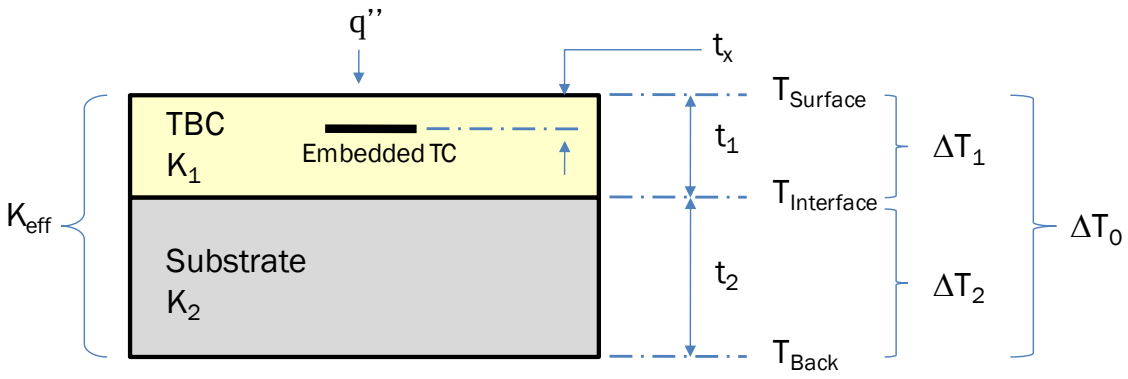

Figure 2-7Diagram of cross section embedded thermocouple system which consist of a substrate, a top coat of TBC and the embedded thermocouple.

Further manipulation gives:

$$\Delta T_1 = \frac{q'' \times t_1}{K_1}$$ Equation 2-12

$$\Delta T_2 = \frac{q'' \times t_2}{K_2} \quad \text{Equation 2-13}$$

$$\Delta T_1 + \Delta T_2 = q'' \times \frac{t_1 + t_2}{K_{eff}} \quad \text{Equation 2-14}$$

$$\frac{q'' \times t_1}{K_1} + \frac{q'' \times t_2}{K_2} = q'' \times \frac{t_1 + t_2}{K_{eff}} \quad \text{Equation 2-15}$$

Therefore

$$K_{eff} = \frac{K_1 K_2}{t_1 K_2 + t_2 K_1} \quad \text{Equation 2-16}$$

To calculate $T_{interface}$

$$\frac{\Delta T_1}{\Delta T_1 + \Delta T_2} = \frac{t_1/K_1}{\frac{t_1 + t_2}{K_{eff}}} \quad \text{Equation 2-17}$$

$$T_{Interface} = T_{Surface} - \Delta T_1 \quad \text{Equation 2-18}$$

With a similar approach we derivate Thermocouple ($TSTC_1$) temperature

$$\frac{T_{Surface} - T_{TSTC\ 1}}{T_{Surface} - T_{Interface}} = \frac{t_x}{t_1} \quad \text{Equation 2-19}$$

Thus

$$T_{TSTC1} = T_{Surface} - \frac{t_x}{t_1} \times \left(T_{Surface} - T_{Interface}\right) \quad \text{Equation 2-20}$$

2.4 Results and Discussion

2.4.1 Thermoelectric sensitivity of TSTC

Thermal spray thermocouples (TSTC) were tested up to 900 °C in a furnace and proved to be durable and provided a stable reading. The temperature readings were repeatable and linear in the temperature range of interest, which means that there is little effect (oxidation, sintering, etc.) on the film material during the duration of the test (it is accepted that exposure for extended periods at the test temperature will induce oxidation of the films). An actual photograph of a set of TSTC deposited on YSZ is shown in Figure 2-8.

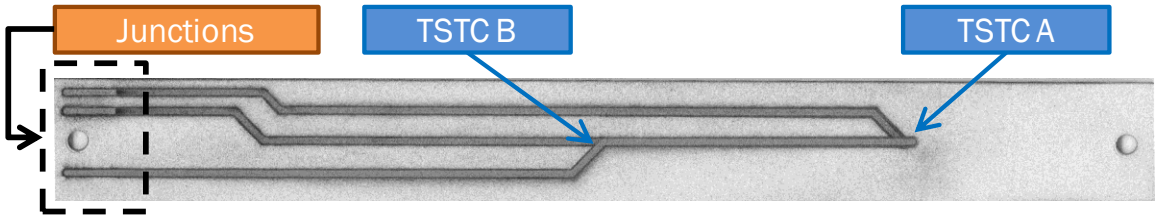

Figure 2-8 Thermal sprayed thermocouples deposited on YSZ base layer.

TSTC-A and Ref.TC-A don't overlap when the voltage output is plotted against the reference temperature (Figure 2-9). Since the Seebeck coefficient is nominally 41.1 μV/°C for the type-K thermocouple, slight deviation from this value causes the reading to be imprecise. However, a linear fit, or in this case polynomial, can be applied to the curve. The Seebeck coefficient for the TSTC when using a linear fit is 39.1 μV/°C with a regression factor of 0.9933. However, the best fit is with a polynomial fitting to $TSTC_{Temp.} = -0.216X^2+34.5x$ (where x = TSTC output in milivolts [mV]) with a regression factor of 0.9996 from room temperature to 950°C. In both cases TSTC yielded a response comparable to the commercial type-K thermocouple and similar with the results reported in literature [3].

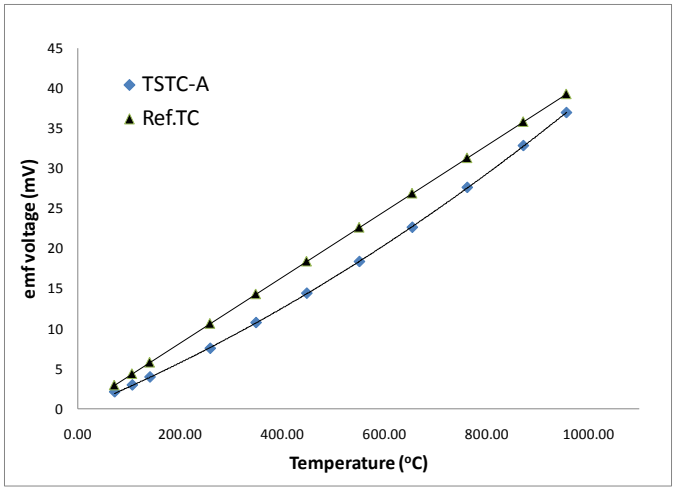

Figure 2-9 Seebeck measurement on a thermal sprayed thermocouple

2.4.2 Challenges during testing of TSTC

Deposited thin coatings films are subject to degradation due to the elevated temperatures at which they are tested and implemented. The mismatch in coefficient of thermal expansion (CTE) of the films and the embedding media, oxidation of the film at high temperatures as well as other factors contribute to this. Two samples sprayed with condition 2 suffered failure of the film; one delaminated after a short test at 500 °C in an oven, the second one, during overcoat deposition of APS YSZ as can be seen in Figure 2-10 and Figure 2-11.

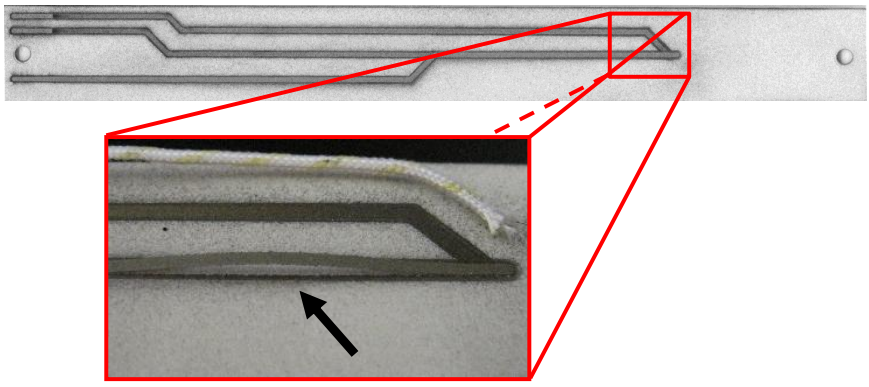

Figure 2-10 Delamination of the conductor film after heat treatment at 500 °C

In addition to the stresses at which the films are subject due to quenching and peening during spray, they have to bear especially during heat cycling with the differences in CTE of film and substrate, the adhesion of the film on the YSZ base layer and additional strain from bending of the substrate-base layer (composite beam). The lower temperature and faster particle velocity of condition 2 induces less wetting and lower splat-splat bonding due to a lower molten state of the particle than condition 1.

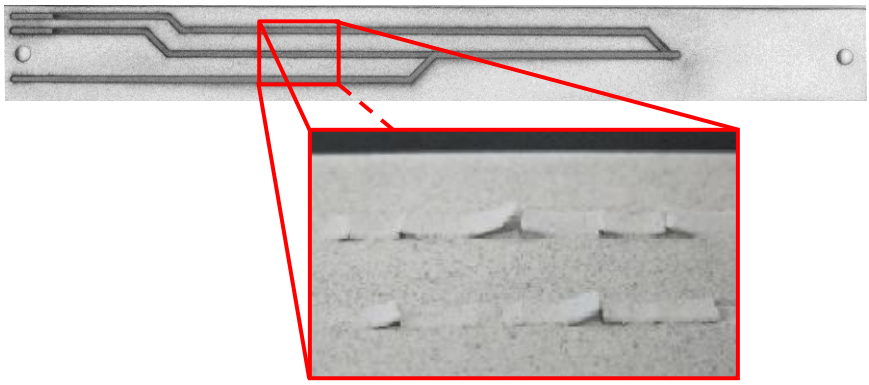

Figure 2-11 Delamination of the conductor film during spraying of YSZ overcoat.

In order to mitigate the effect of intrinsic stresses in the system, a process condition that induce higher temperature and lower velocity to the particles with an overall effect of higher residence time in a hotter plume, hence higher degree of melting (condition 1).

2.4.3 In-Situ Temperature Sensing during Plasma Spray

In-situ temperature sensing is of great importance, especially when the substrate or the coating itself is sensitive to property degradation when exposed to high temperatures. These issues occur during the deposition of the coating or during operation of the component. It is the case of carbide-containing coatings, steels, titanium alloys among other metals. The case that is attaining to this study, gas turbine components.

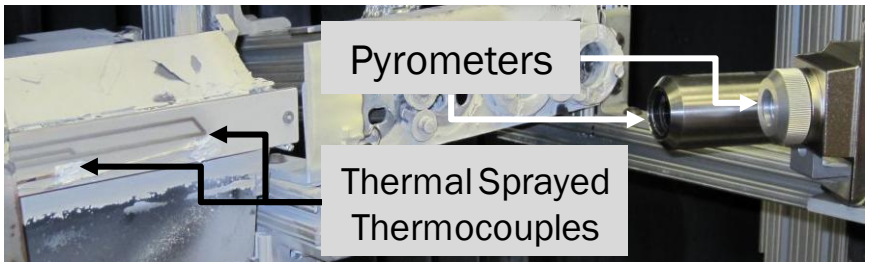

Figure 2-12 Setup for spraying top coat on thermal prayed thermocouples. Sample is mounted on ICP sensor mount (left), two infrared pyrometers are installed (right)

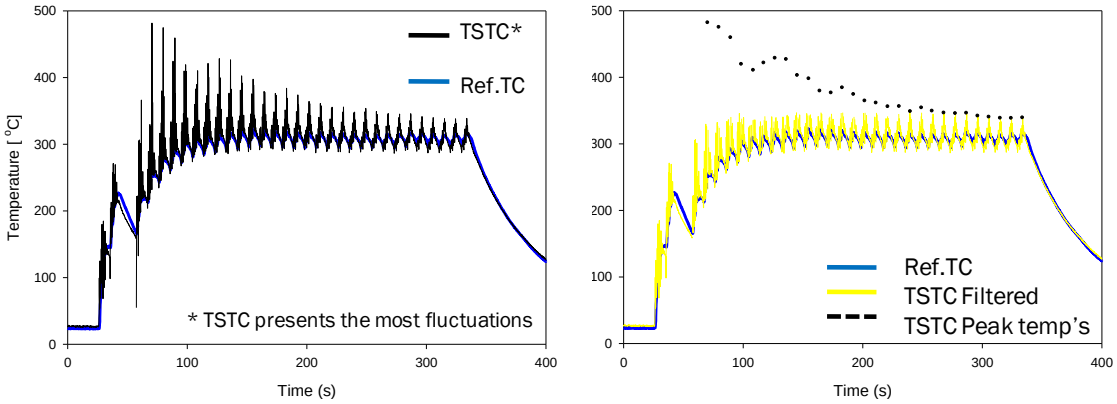

Figure 2-13 In-situ temperature sensing during APS thermal spray (post processed to account for TSTC Seebeck). Left, raw data from the TSTC and Ref.TC. Right, processed data to separate peak temperatures from average, Ref.TC is shown as well.

The swivel of the torch across the sample's surface generates fluctuations in temperature, reaching a maximum when the flame from the torch is right in front of one of the thermocouples. Also, the heat from molten particles is in part transferred to the coating system upon impact. Furthermore, as the TBC thickness increase a reduction in the peak temperature is observed Figure 2-13. This itself is a great example of how the TBC helps providing thermal barrier reducing the temperature of the underlying metallic substrate, i.e., by creating a thermal gradient between the hot face and the metal-ceramic interface. Figure 2-14 show an embedded TSTC a thin layer of YSZ was sprayed for illustration purposes.

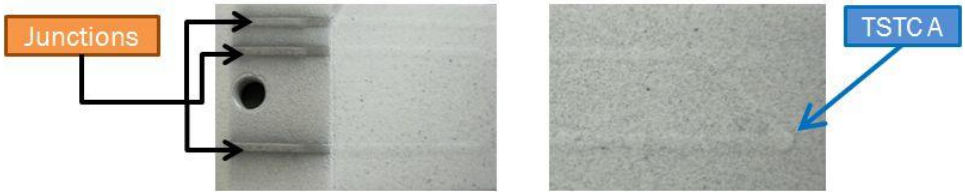

Figure 2-14 Embedded thermocouples with a thin (50 μm) YSZ overcoat

2.4.4 Temperature Sensing Under High Heat Flux Conditions: Heat Flux

Temperature gradients drive heat flowing from a zone of higher temperature to lower one. This heat-transfer process is of great importance in engineering components, especially those subject to temperatures at which degradation of the material occur. There are three mechanisms in heat transfer, i.e., convection, conduction and radiation. In engineering processes it is usual to find that heat transfer occur simultaneously in all three modes. Convective heat transfer inside the coating is non-significant [35] due to the small size of the pores and cracks.

To accurately model the heat flux, precise estimates of the coating thermal conductivity of the TBC at various temperatures of interest are required, and also systematically after various aging periods (heat treatment). In this work, relatively short duration test are carried out below 1000 °C, therefore annealing of the TBC is not expected to occur.

Two embedded TSTC with 147μm (TSTC1) and 501μm (TSTC2) YSZ overcoat were tested in a burner rig (Figure 2-15) using an oxyacetylene flame. The overcoat layer of YSZ was sprayed with the process parameter shown in Table 2-2. The test results show that the TSTC follow the trend on heating and during the stable segments. Small temperature fluctuations were observed Figure 2-16, the pyrometer also presents a similar response therefore it might be attributed to heat input disruption from flame conditions variation. It seems that

the magnitude of these fluctuations is attenuated by the TBC since the TSTC shows slightly smaller fluctuation than that from pyrometer.

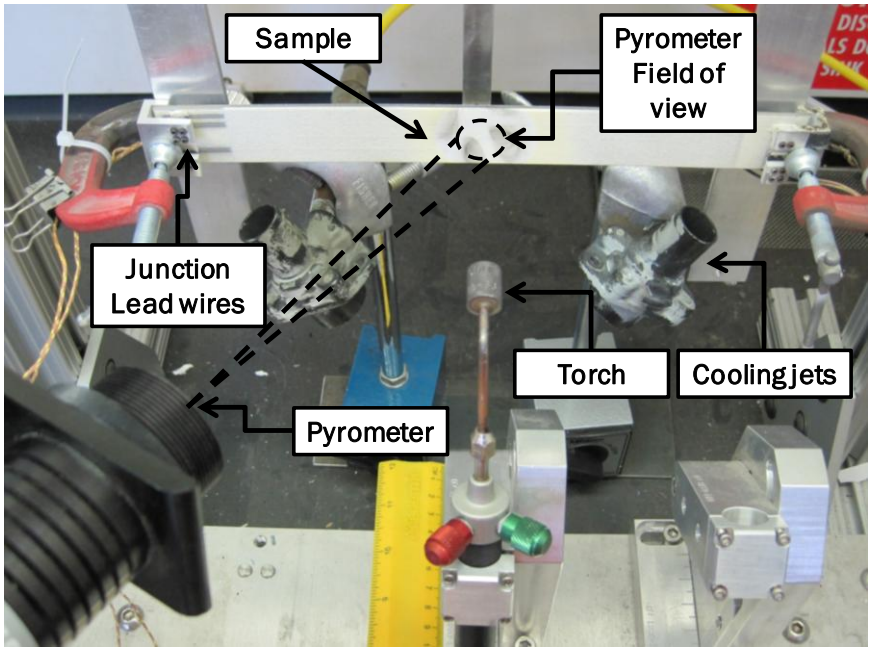

Figure 2-15 Burner rig test setup.

The modeled temperature agrees well with the temperature reported by TSTC2 (thicker overcoat) but is higher for TSTC1 (thinner overcoat).

The difference between model and the experimental results for temperature could be attributed to a slight difference in the Seebeck of TSTC1. Slight variations of the Seebeck may occur when the material is subject to high temperatures and/or harsh environments. Such deviation from linearity with exposure time at high temperatures can be investigated to incorporate it in the Seebeck coefficient for this system. Embedded thermocouples advantages over pyrometers are many since they are less prone to be affected by instantaneous fluctuations from the heat source.

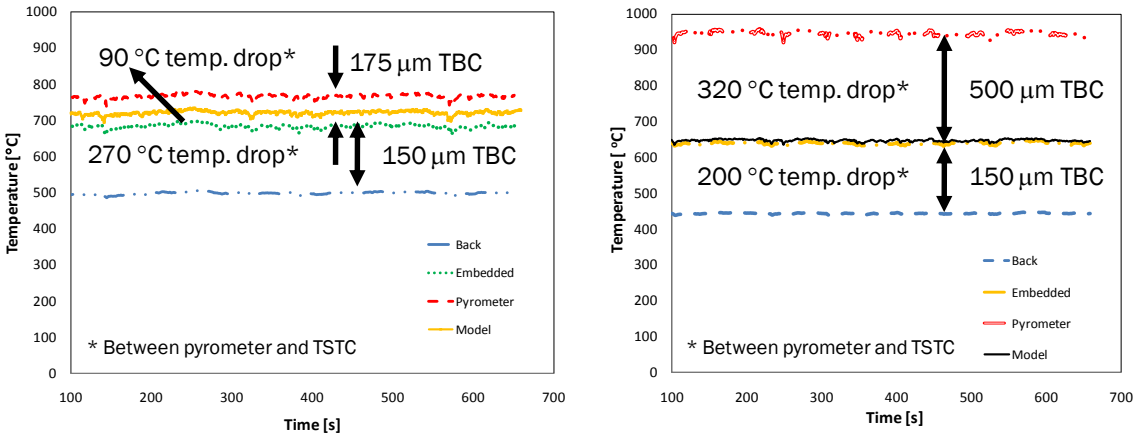

Figure 2-16: Burner rig test performed on two embedded TSTC. TSTC1 with 130µm overcoat (left), TSTC2 with 500µm overcoat (right).

2.5 Summary and Conclusions

Thermal sprayed thermocouples (TSTC) have been successfully synthesized and tested to over 1000 °C showing that they are robust and can be fabricated in an industrial environment. The TSTC can capture the temperature variation during deposition of the TBC and provides in-situ sensing for thermal spray. The feasibility to embed them in the TBC allows for the creation of sensors for in-situ measurement of temperature during plasma spray and to produce a heat flux sensor. Difficulties such as delamination were conquered to successfully deposit the TSTC and embedded in a TBC.

Measured output between the TSTC and the reference type-K thermocouple shows good agreement; It can measure coating internal temp under high heat flux conditions which are similar to service conditions. Embedded TSTC follow the temperature trend of the system and agree well with the calculated temperature from the model.

Chapter 3 Percolation Study in Thermally Sprayed Al_2O_3-Ni Resistor Composites

3.1 Introduction

Two component composite systems (composite-cermets and functionally graded) find extensive application in wide range of systems (structural, wear, corrosion, electronics, etc.) They have also found applications as functional materials such as metal-ceramic resistors, magnetic sensors, etc.

Sensor development has been studied extensively in the past decade. Commonly used resistor composites require the use of controlled atmosphere and in some cases vacuum chambers, usually long and complicated processing in addition to high cost of production. Another type of sensor is made out of magnetic composites e.g., Mn-Zn-Ferrit (MZF) which are suitable for a wide range of applications such as inductors and transformers, EMI, magnetic recording, microwave, magnetorestrictive sensors, etc. [36-39]. The processing techniques include among the most common for fabrication of thin film composites: sputtering, pulse laser deposition, CVD, and for larger components sintering. All those methods mentioned before involve complex preparation and several processing issues such as reaching electrical percolation.

Different authors have shown that thermal sprayed metal-ceramic composites exhibit a much lower percolation threshold than conventional systems [40-44], this is due to the anisotropy of the microstructure which is based on thin disk-shaped splats [45]. Liang[40] has developed a model to correlate the flattening ratio (which is greatly influenced by the process and spray parameters used) to the percolation threshold in Mn-NiCo-Ferrite metal-ceramic composite system.

To achieve electrical percolation threshold (*Pc*) in composite systems based on spheroid particles, large amounts of the metallic component is required since the *Pc* in such systems is usually reached at 33vol%. Thermal spray has been proposed as a method of fabrication of such composites given the large anisotropy of the materials deposited with this process [45] which allows for a reduction in the metal content needed to reach *Pc*. Thermal spray can be used for the production of metal-ceramic composites in a cost effective way.

"There are many physical situations in which a fluid spreads randomly trough a medium. Here fluid and medium are abstract terms to be related to the context" [46], and in our case it means electrons moving through the coating. As defined by D. Stauffer[47], the percolation threshold p_c is that concentration at which an infinite network appears in an infinite lattice. For all $p > p_c$ one has a cluster extending from one side of the system to the other, whereas for $p < p_c$ such no such infinite cluster exists. The change in conductivity from insulating to conducting behavior of a composite is not linear and it's called percolation. The critical value is called percolation threshold

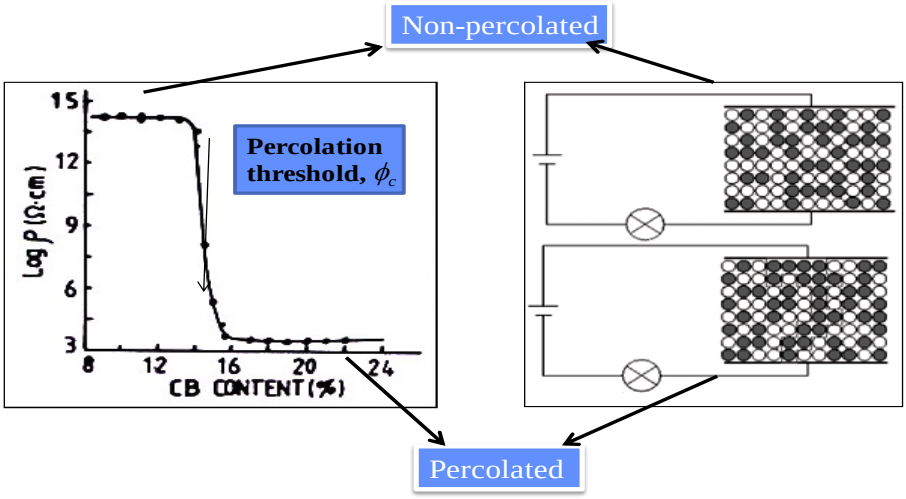

Figure 3-1: Illustration of electrical percolation. Left, resistivity of a ceramic-carbon black (CB) composite system as a function o volume fraction of CB. Right, top, below percolation threshold; bottom, above the percolation threshold where a short circuit is created by the interconnecting conductor particles (CB) [40].

The resistivity of metal-insulator composites depend critically on its microstructure and composition. The percolation threshold (p_c), depends on the resistivity of each phase in the composite, the size and shape and orientation of the particles. Thermal sprayed coatings are built on a splat basis (disk-shaped units) with a significant aspect ratio, therefore highly anisotropic microstructures result. Several studies have pointed out that in highly shape-anisotropic system, the percolation threshold can be as low as a few volume percent of the metallic phase, contrasting to around 30 percent in the classic spheroid dispersed systems [40, 47, 48].

3.1.2 Anisotropy in thermal sprayed metal-ceramic composites

As a result of the process characteristics, the coatings produced by thermal spray have a lamellar anisotropic microstructure. Physical properties such as elastic modulus, thermal conductivity, resistivity among others also exhibit anisotropy (different through the thickness of the coating versus that in the plane of the coating). Furthermore, since the many variations of thermal spray processes produce significantly different coating microstructures, the coatings may also exhibit a variation in anisotropic physical properties from process to process [45].

Shafiro and Kachanov [48] have shown that the properties of an inhomogeneous media can be described in terms of volume of the inclusions (pores, cracks, oxides, etc. Figure 3-2) only in the special case when all the inclusions possess the same characteristic property (e.g., conductivity), and have the same aspect ratio. Thermal spray coatings are far from this special case; the coatings contain not only various types of defects but they also have a large distribution of the shape, size and orientation.

The HVOF deposits consist of much thinner splat layers with fewer and substantially narrower interlamellar pores as compared with APS ones. Due to relatively lower temperatures and higher velocities involved in HVOF process, less oxidation and volatilization occurs. In addition, these factors influence the molten particles in-flight condition in such a way that most of the oxide formed in the process remains distributed within the interior of the splats in contrast to the APS deposits where most of the oxide is found segregated in the interface region.

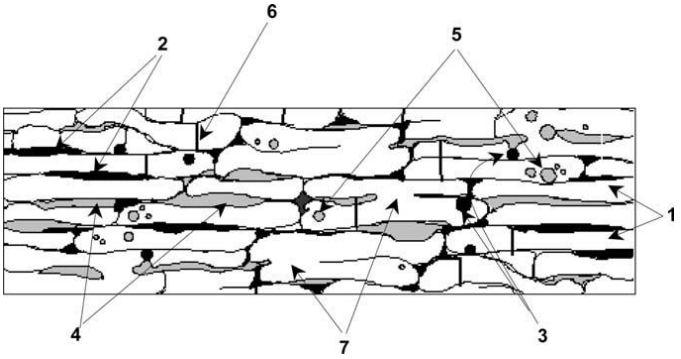

Figure 3-2 Schematic representation of the microstructural features associated with typical thermal spray coatings: (1) splats, (2) interlayer (or interlamellar) pores/cracks, (3) globular pores, (4) interlayer oxide precipitates, (5) intra-layer oxide precipitates, (6) intra-splat cracks, (7) regions of true contact (metallurgical junction) [45].

3.1.1 Novel resistor composites for sensor applications using thermal spray

Thermal spray has been considered for electronic applications for more than two decades, some of these applications include ferrites, magnetic alloys and resistors[49]. Thermal spray advantages in processing include low substrate temperature (as opposed to conventional methods), high throughput production capability, cost efficiency and minimizing the reaction between ceramic and metallic phases. The microstructure and composition of metal-insulator composites influences dramatically its electrical properties, e.g. resistivity. The

percolation threshold depends on the resistivity, size, shape and orientation of each phase in the composite.

In a recent work by Liang [40] and attempt to make MnZn-NiCo ferrite composite thick films by thermal spray led to the creation of a model to predict percolation threshold as a function of flattening ratio.

3.1.3 Interest in thermal sprayed metal-ceramic composites

Magnetic and resistive metal-ceramic composites are widely used in the electronic industry due to their unique properties. In this regard, thermal spray poses as an interesting processing technology towards synthesis of such composites. Sampath [50] made composite resistors via HVOF by mechanically mixing Ni-20Cr and Al_2O_3 and obtained electrical percolation threshold at 8 vol%NiCr as is presented in Figure 3-3.

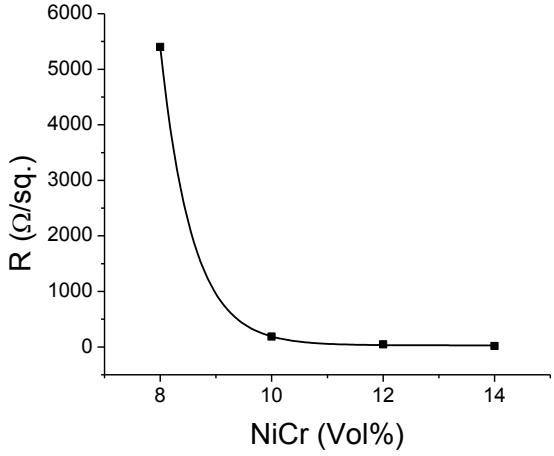

Figure 3-3 Resistivity of thermal sprayed cermet resistors obtained from NiCr-Alumina composite with various volume fractions [50].

A plasma sprayed MnZn-NiCo ferrite (MZF-NiCo) was studied by Liang [40] with the purpose of exploring the potential of plasma spray in making

magnetic composites with application in magnetostrictive and magnetorestrictive sensors and planar inductors. One of the results from the later study is a model that correlates the flattening ratio of splats to the percolation threshold for the composite. Table 3-1 and Figure 3-5.

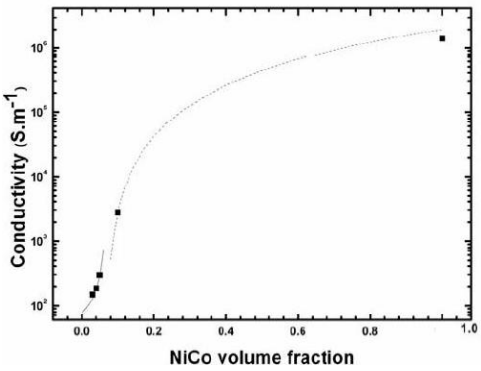

Figure 3-4 Electrical conductivity of plasma sprayed MZF-NiCo composite as a function of NiCo volume fraction. [40]

Numerous difficulties arose during processing such as powder feeding issues due to the use of non customized powders, significant changes in composition of the materials being deposited. Therefore, a more manageable system with good processing characteristics, materials availability and that could be sprayed with various processes e.g. APS, HVOF, flame spray was chosen to understand the percolation as a function of processes and process conditions.

Table 3-1: Flattening ratio and percolation values for APS sprayed MZF

Feedstock	Process	Flattening ratio	Percolation (Vol%)
MnZnFe-NiCo	APS	2.4	7

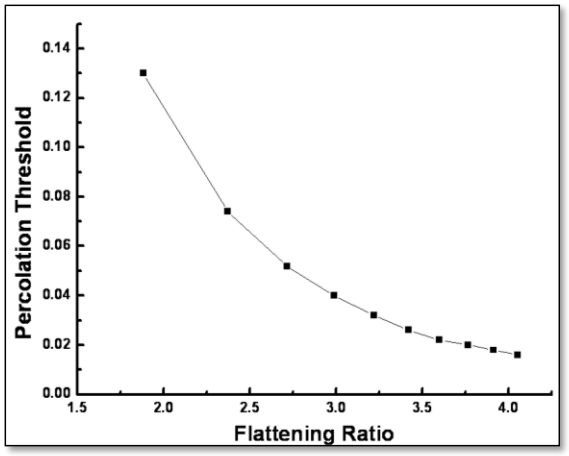

Figure 3-5: Model of percolation threshold as a function of flattening ratio [40].

3.1.4 Statement of the problem and objectives

Thermal spray process has the ability to deposit a wide variety of materials and in some cases the substrate can be kept at relatively low temperatures (100-200 °C) is a great advantage. However the imperfections in the structures yield poor properties and limited functionality of composites for the electronics industry [49]. One of the challenges of today comes from the fact that the irregularities and the intrinsic defects makes it complicated to model and fully understand the effect they this imperfections have on the composite.

The electrical percolation behavior of thermal sprayed composites is significantly different than traditional mixed phase composites giving the aspect ratio of the particles involved which are dependent to great extent on the process and feedstock powders used. Composition and properties are closely related in this kind of composites therefore it is of critical importance to control them. Thermal spray process introduces changes in composition due to its thermal nature and a method to compensate for has to be developed.

How the process parameters affect the percolation threshold in thermal sprayed metal-ceramic resistors needs better understanding, as well as the developing of not only process strategies but also methods of characterization other properties. This study will focus on understanding the influence of process and parameters on the flattening ratio and therefore on the percolation threshold.

It was also shown that Mn-Zn-Ferrite (MZF) can be processed using APS and find applications within the electronics industry.However, given the technical difficulties linked to the MZF-NiCo system (oxidation, flattening ratio, deposition efficiency, flowability, segregation), a simpler system that has been well characterized [51] and has shown great possibilities on applications were graded materials are a suitable [52-55] given its electrical insulation or enhanced mechanical properties was chosen to validate the abovementioned model. The chosen system composed of alumina (Al_2O_3) and nickel (Ni) can be used both by HVOF and APS processes providing for a wider spectrum of particle velocities that are the main variable influencing percolation threshold.

It is important to understand how percolation works in sprayed two component systems and to make a tight relation between flattening ratio, processing parameters and electrical properties.

3.2 Experimental Procedure

3.2.1 Synthesis of thermal sprayed composite resistors

Both APS and HVOF have been implemented for processing of composite metal-ceramic materials with the purpose of making resistor and magnetic composites. As mentioned before NiCr- Al_2O_3 composite resistor with a low percolation threshold was successfully produced by thermal HVOF, also MZF-NiCo was sprayed using APS with interest in applications as a magnetic sensor. The later study encountered issues during processing and due to its complex composition and microstructural characteristics. An interesting characteristic of each one of these processes is the particle velocity, HVOF being two to five times faster than APS. A direct consequence of this characteristic is the different flattening ratios obtained in each case. The later being the reason to select both APS and HVOF to spray the composites in the present study.

3.2.1.1 APS sprayed coatings

APS coatings were prepared using an F4 torch (Sulzer Metco, Westbury, NY, USA) with 8mm and 6mm nozzle, spraying parameter are presented in Table 3-3. Nickel (56F-NS from Sulzer Metco, Westbury, NY, USA), Al_2O_3 (AI-1110HP from Praxair Surface Technologies, Indianapolis, IN, USA) and Al_2O_3 (HW-153 Saint Gobain, Worcester, MA, USA) powders were prepared, Table 3-5presents complete information of the powders used.

Three batches (sets') of powder blends with nickel concentrations ranging from 0 (pure alumina), to 100 vol%Ni (pure nickel) were prepared, see Table 3-2 for the full description of the compositions used.

Table 3-2 Concentration of nickel used with APS sprayed composite

Set #	Nozzle	Concentration of Ni in Al_2O_3-Ni blends (vol%)								
1	8mm	0.00	3.00	4.50	6.00	9.00	-	-	-	-
2	6mm	0.00	3.00	4.50	6.00	9.00	-	-	-	100.00
3	6mm	0.00	0.11	0.29	0.65	1.01	1.37	1.73	2.00	-

Given equipment limitations to reach such low nickel concentrations in feeding of powder set #3 it was necessary to use a dual feeding system. The first one (feeder A) contained pure alumina powder, while the second (feeder B) contained a blend of alumina and 2 vol% nickel. Both feeders were operated simultaneously to obtain the desired compositions.

Table 3-3: Spraying conditions for APS sprayed coatings

Gas Flows			Energy		Particle State	
Argon	Hydrogen	Carrier (Ar)	Current	Voltage	Temperature	Velocity
SLM	SLM	SLM	A	V	°C	m/s
47.5	6.2	3.5	550	61.6	2842	162
F4 torch, 8mm Nozzle. Traverse torch velocity 0.5 m/s. Feed rate 30 g/min.						

3.2.1.2 HVOF sprayed coatings

Coatings were prepared by HVOF using an HV-2000 torch (Praxair Thermal Spray Products, Appleton, WI) with a 22 mm nozzle, spraying parameters are presented in Table 3-4. Nickel (56F-NS from Sulzer Metco, Westbury, NY, USA) and Al_2O_3 (AI-1110HP from Praxair Surface Technologies, Indianapolis, IN, USA) powders were mixed thoroughly previous to be inserted in the powder feeder, Table 3-5 presents complete information on the powders used. Batches with nickel concentrations of 0 (pure alumina), 1.5, 3.0, 4.5, 6.0 and 9.0 vol% were prepared.

Table 3-4: Spraying conditions for HVOF sprayed coatings

Gas Flows			
Fuel	Oxygen	Carrier	Fuel/oxy ratio
SCFH	SCFH	SCFH	
165	600	45	0.28
Gas Pressures: Fuel (propylene) 110 psi, Oxygen 160 psi, Carrier (hydrogen) 140 psi. Spray distance 152 mm. Traverse torch velocity 0.75 m/s. Feed rate 15 g/min			

Table 3-5: Feedstock used in APS and HVOF processes

Material	Production Method	Nominal Composition	Size Range	Morphology
Saint Gobain HW 153	Sintered	99.3% Al_2O_3	-45/+11 μm	Irregular
Praxair Al-1110HP	Sintered	99.3% Al_2O_3	-22/+5 μm	Irregular
Sulzer Metco 56F-NS	Precipitated	99.5% Ni	-45/+10 μm	Spheroidal

Table 3-6 Particle state vs. nickel content (Accuraspray)

	Nickel content (vol%)					
Particle State	0.0	1.5	3.0	4.5	6.0	9.0
Temperature (°C)	3150	3000	2700	2600	2500	2600
Velocity (m/s)	820	600	590	570	560	600

3.2.2 Electrical conductivity measurements

Electrical conductivity was calculated from the measured resistivity. For the in-plane (IP) direction, square samples (25x25 mm^2) were prepared into a freestanding coating by grinding away the substrate, the specimen was then polished and mounted on an insulating holder. Lead wires were attached to each corner and the Van der Pauw method was used to calculate electrical resistivity and ultimately the electrical conductivity. To measure the through thickness resistivity (TT), a square sample (25x25 mm^2) was used and a silver paste electrode with an area of 20x20 mm^2 was applied to the coating surface. The metallic substrate (AISI 1018 steel) was used as the counter-electrode. Lead wires were then connected to both electrodes, a current was passed through the specimen and the resulting voltage was measured. From the corresponding I-V curve the resistance and ultimately the conductivity was calculated

3.2.2.1 In-plane electrical conductivity

The Van der Pauw method was used to calculate the electrical conductivity of freestanding coating samples. It is a more general method where

the freestanding sample can be treated as a semi-infinite 2-dimensional substance. The measurement requires that four ohmic contacts be placed on the sample. The contacts are numbered from 1 to 4 in a counter-clockwise order, beginning at the top left contact as shown in Figure 3-6.

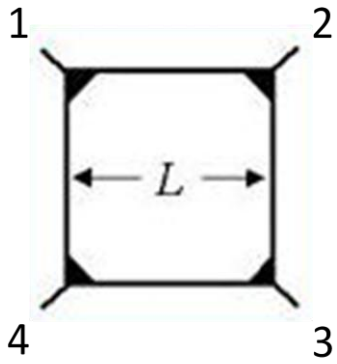

Figure 3-6: Van der Pauw method, specimen layout.

The sheet resistance of samples is related to $R_{12,34}$ (R_A)and $R_{23,41}$ (R_B) by the Van der Pauw formula:

$$e^{\left(\frac{-\pi R_A}{R_S}\right)} + e^{\left(\frac{-\pi R_B}{R_S}\right)} = 1 \qquad \textbf{Equation 3-1}$$

Then the resistivity can be calculated for a known thickness as:

$$\rho = R_S \times t \qquad \textbf{Equation 3-2}$$

Thus the conductivity is:

$$\sigma = \frac{1}{\rho} \qquad \textbf{Equation 3-3}$$

3.2.2.2 Through thickness electrical conductivity

The electrical resistance of the composite can be calculated from the slope of the I-V curve as follows:

$$\boldsymbol{\rho = R \times \frac{A}{t}}$$ **Equation 3-4**

Where ρ is the resistivity, t is the specimen thickness, A is the area of the silver electrode and R is the resistance measured.

Conductivity = $\boldsymbol{\frac{1}{\rho}}$ **Equation 3-5**

Where R_S is the sheet resistance and R_A, R_B resistance is calculated from the I-V curve

3.2.3 Microstructural examination

A LEO 1550 SEM system was utilized to acquire high-resolution images of the coatings cross-sections. Image analysis of cross sections of the composite coatings was chosen to estimate the volume fraction of the two components and the porosity. Image analysis software (ImageJ, US National Institute of Health) was used to separate the two phases and the porosity (the image was set In the SEM so that the nickel was white, alumina grey and porosity black) and count the area of each. Assuming the area ratio is equal to the volume ratio by taking statistically enough sampling, the content of each component in the composite can be determined. Figure 3-12, Figure 3-10 and Figure 3-11 show the HVOF, APS1 and APS2 composite coatings respectively

3.2.4 Flattening Ratio

Splats were collected by rapidly moving the torch across a preheated (~200 ^{0}C) substrate.

By definition flattening ratio f= *d/D [45]*, as can be seen in the Figure 3-7

Where *d* is the diameter of the splat and *D* is the diameter of the molten droplet before impact. From the conservation of volume between splat and the droplet that formed it, we have,

$$\frac{4}{3}\pi\left(\frac{D}{2}\right)^3 = \pi\left(\frac{d}{2}\right)^2 t \qquad \textbf{Equation 3-6}$$

Where t is the splat thickness

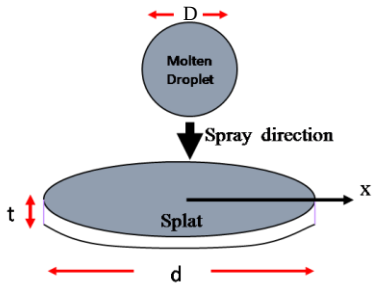

Figure 3-7: Schematic of impacting droplet of molten material and the formed splat

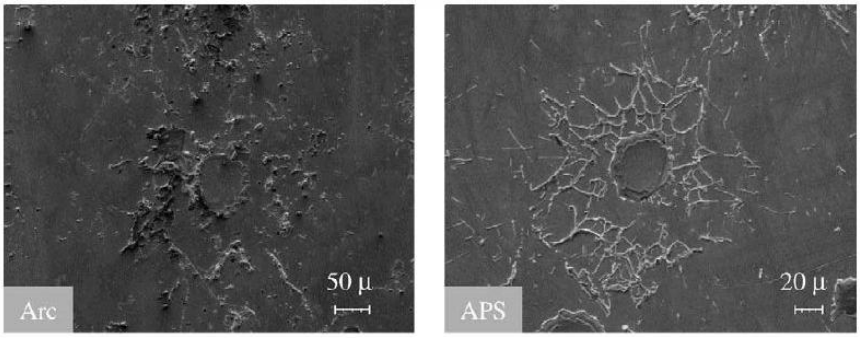

Figure 3-8: Morphologies of Ni-5wt.%Al splats produced with different techniques. (taken with permission of the author)

3.3 Results and Discussion

For the composite system studied a homogeneous distribution of the metallic phase was achieved within the alumina. In plane and through thickness conductivity was measured and the electrical percolation was achieved. Image analysis and white light interferometry was performed on cross-section and single splats respectively to calculate actual content of metal in the composite ad flattening ratio. Finally the flattening ratio was linked to the electrical percolation using a previously developed model

3.3.1 Microstructural evaluation

Microstructures from set1 and set2 show wavy splats rather than flat-elongated ones, high porosity and oxide content. It seems a rough microstructure which from the point of view of deposition means that incoming particles impact a surface that could limit its freedom to spread on the surface and ultimately reduce the flattening ratio.

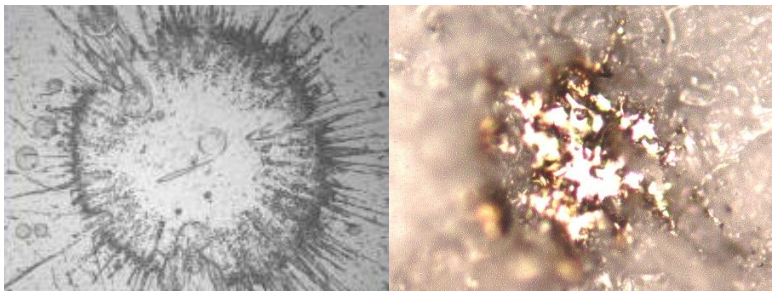

Figure 3-9 Nickel splats collected on a polished stainless steel substrate (left), and on sprayed (APS) alumina (right).

Figure 3-9 shows nickel splats collected on a polished stainless steel substrate, and on APS sprayed alumina. These images allow the comparison of splats between the two cases; it's apparent that the rougher surface of sprayed alumina restricts the spreading and affects the flattening ratio. Measured diameters over several splats on polished stainless steel and sprayed alumina are 125 μm and 107 πm respectively.

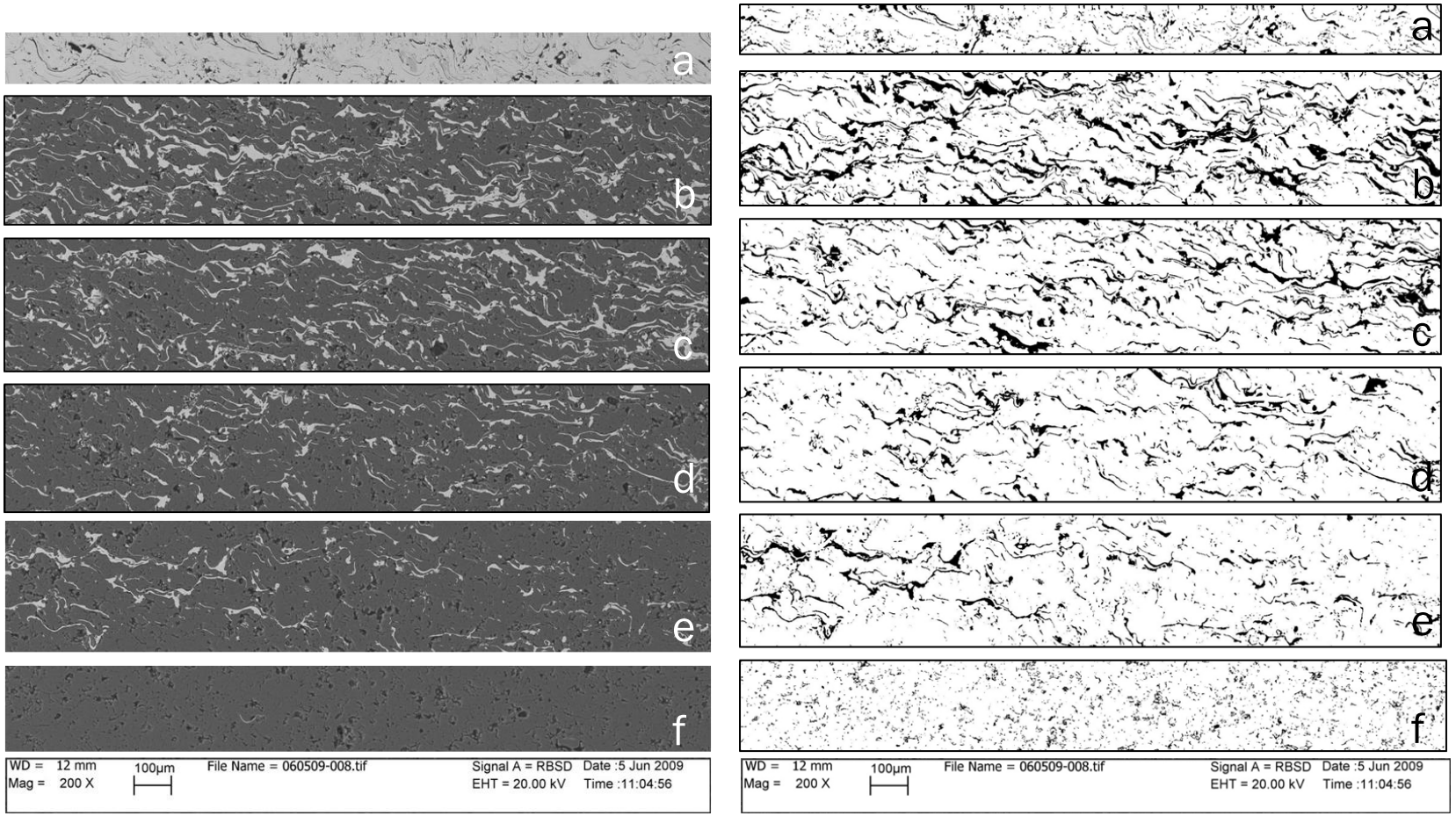

Figure 3-10 APS set1 composite coatings SEM (left), Image analysis binary (right). Nickel volumetric concentration in original blend as follows: a) 100, b) 9.0, c) 6.0, d) 4.5, e) 3.0, f) 0.0 vol% Ni.

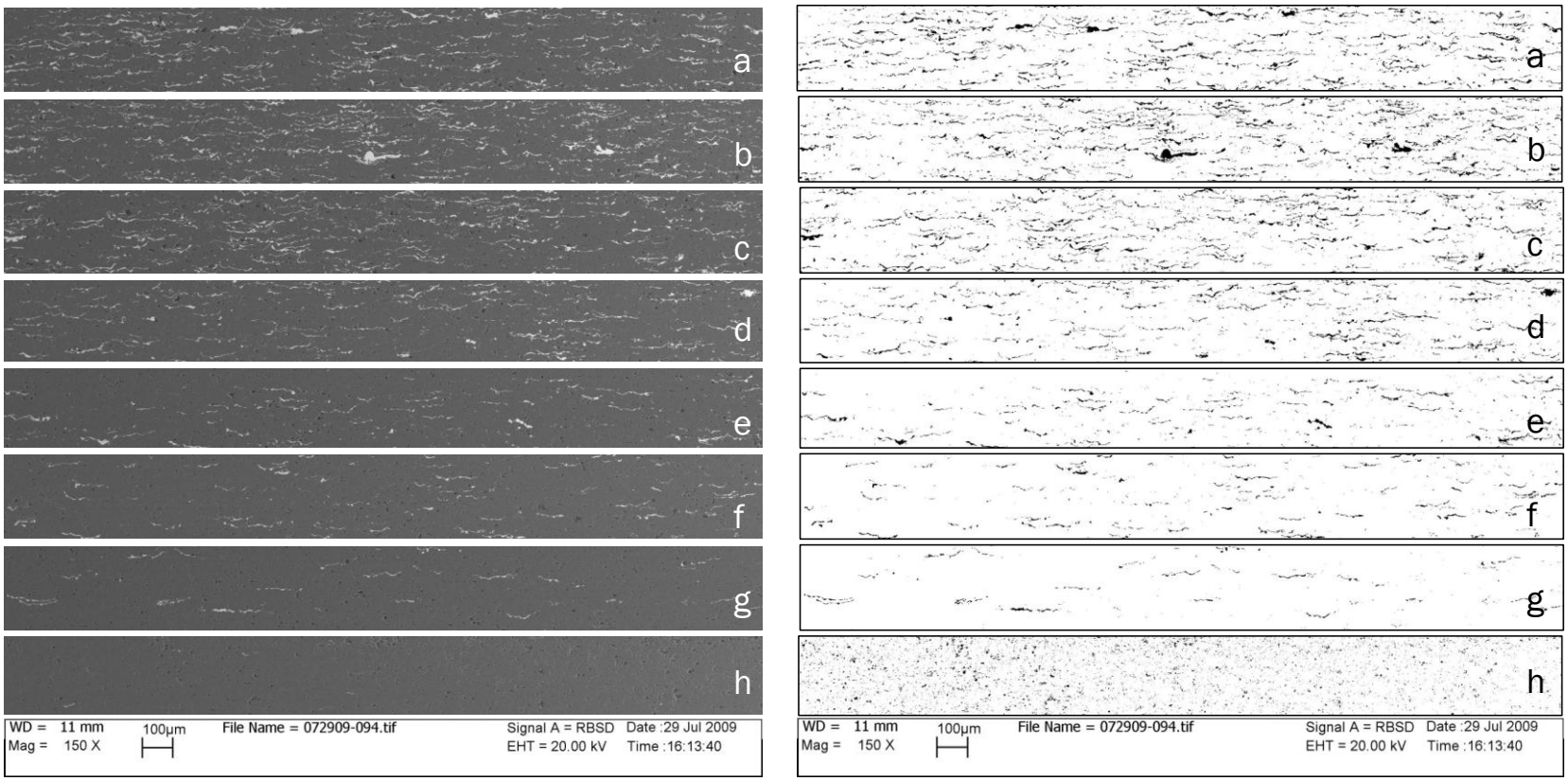

Figure 3-11 APS set2 composite coatings SEM (left), Image analysis binary (right). Nickel volumetric concentration in original blend as follows: a) 2.0, b) 1.73, c) 1.37, d) 1.01, e) 0.65, f) 0.29, g) 0.11, h) 0.0 vol% Ni

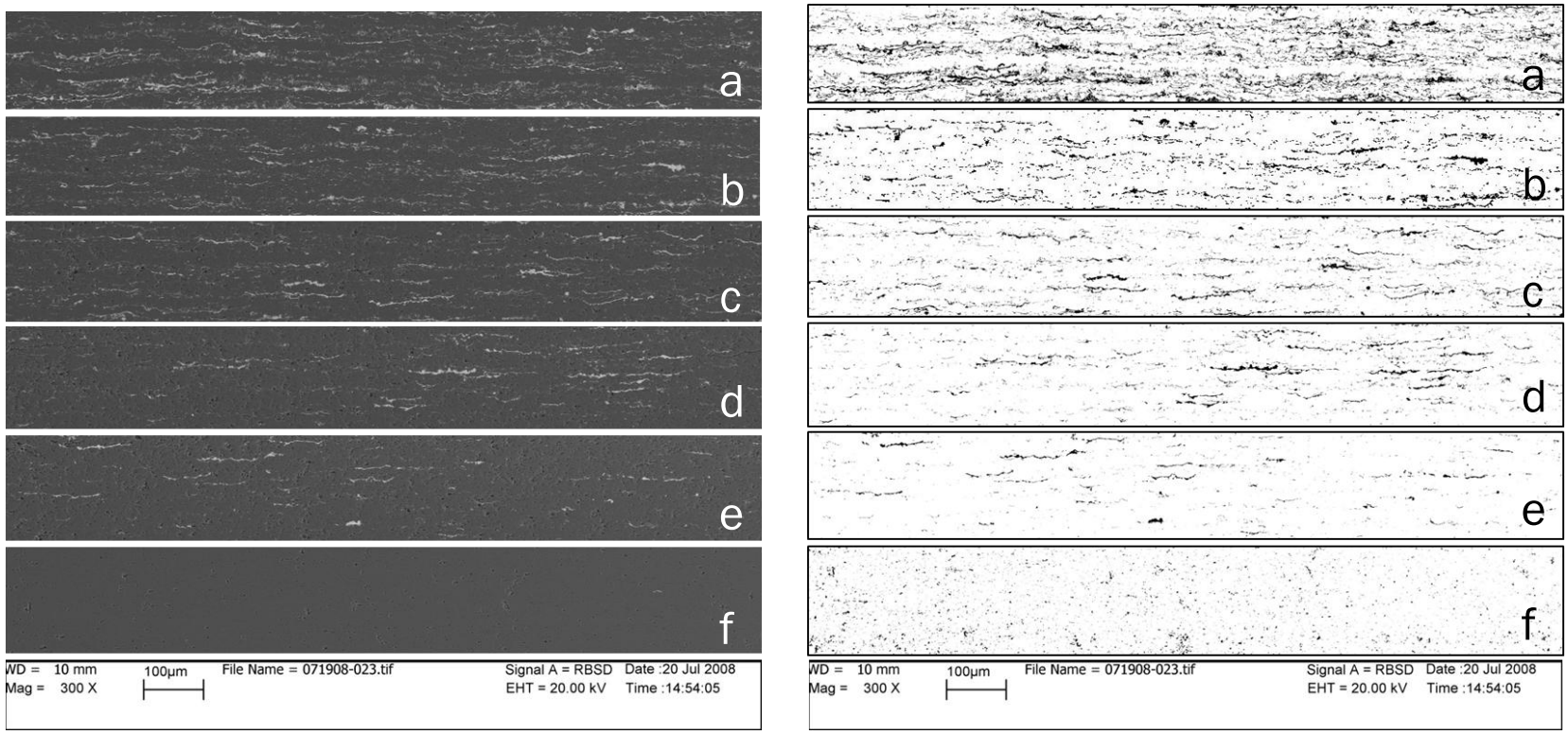

Figure 3-12: HVOF sprayed composite coatings SEM (left), Image analysis binary (right). Nickel volumetric concentration in original blend as follows: a) 9.0, b) 6.0, c) 4.5, d) 3.0, e) 1.5, f) 0.0 vol% Ni.

The splats in the coatings with lower nickel content (0.11 – 0.65 vol% Ni) seem to be isolated in the alumina matrix and no interconnection between splats can be appreciated. This however, starts to change as the content of nickel increase and approaches 2 vol% where splat interconnection is evident.

Figure 3-13 is a higher magnification image of APS sprayed composite set1 and set2 for the same nominal nickel content. In both images the splats have similar wavy appearance.

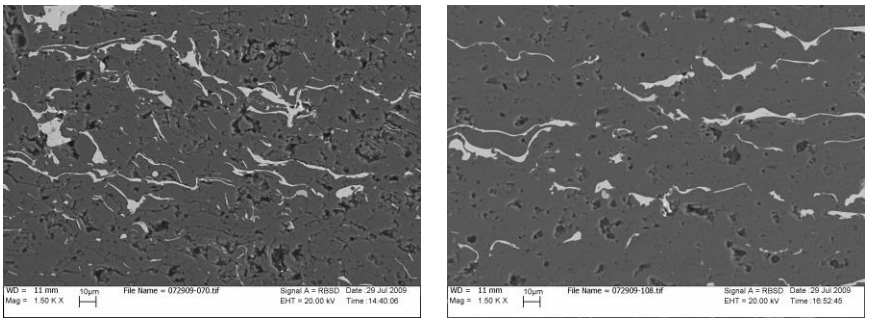

Figure 3-13 APS sprayed composite coatings, left corresponds to set1 and right to set2. Both microstructures have similar splat roughness.

In the HVOF sprayed system the microstructure looks denser with less porosity and oxides than in the APS composite shown before, the splats also look flatter and the roughness in the microstructure observed in the APS sprayed coatings seems no more here. The later can be attributed to the fact that surface roughness tends to be much higher for plasma sprayed coatings than for HVOF ones, the reason for that lays in the much higher particles velocities which are in the order of 600 m/s and 300 m/s for HVOF and APS respectively as shown in Table 3-4 and Table 3-3.

Image analysis show higher than nominal metal content in both APS and HVOF sprayed composites (Table 3-7 and Table 3-8). This clearly indicates that the deposition efficiency of the metal component is higher than the ceramic.

Table 3-7: Nickel volume in HVOF sprayed composite coatings from the image analysis.

Sample Run #	At Injection (Vol%Ni)	Estimate from density (Vol%Ni)	Calculated from IA (Vol%Ni)	Porosity (Vol%)
480	0.00	0.00	0.00	4.1
353	1.50	3.07	3.29	3.8
351	3.00	5.01	6.50	5.2
355	4.50	5.34	4.50	4.7
357	6.00	6.29	6.93	5.7
479	9.00	11.20	13.08	3.5

Table 3-8 Nickel volume in APS sprayed composite coatings from the image analysis.

Sample # Run #	At Injection (Vol%Ni)	Estimate from DE (Vol%Ni)	Estimate from density (Vol%Ni)	Calculated from IA (Vol%Ni)	Porosity (Vol%)
1179	0.00	0.00	0.00	0.00	3.45
1175	0.11	0.36	0.68	0.74	2.77
1176	0.29	0.72	2.03	1.42	3.12
1174	0.65	1.44	2.70	1.90	3.98
1177	1.01	2.14	2.93	3.21	5.18
1173	1.37	2.85	3.60	4.60	3.22
1178	1.73	3.55	2.93	5.01	3.68
1172	2.00	4.24	5.63	5.25	3.04
1129	3.00	6.30	4.10	7.70	4.37
1130	4.50	9.30	7.70	9.70	5.63
1131	6.00	12.2	11.3	13.8	6.05
1132	9.00	17.7	14.6	17.9	4.13
1133	100	100	100	100	4.31

3.3.2 Conductivity in TS metal-ceramic composites

Conductivity in APS 6mm composites show a clear percolation threshold (P_C) at 5.25vol%Ni, anisotropy is also evident between the in-plane (IP) and though thickness (TT) directions Figure 3-14. Higher conductivity is observed in the IP vs. TT directions (anisotropy) for compositions above P_C.

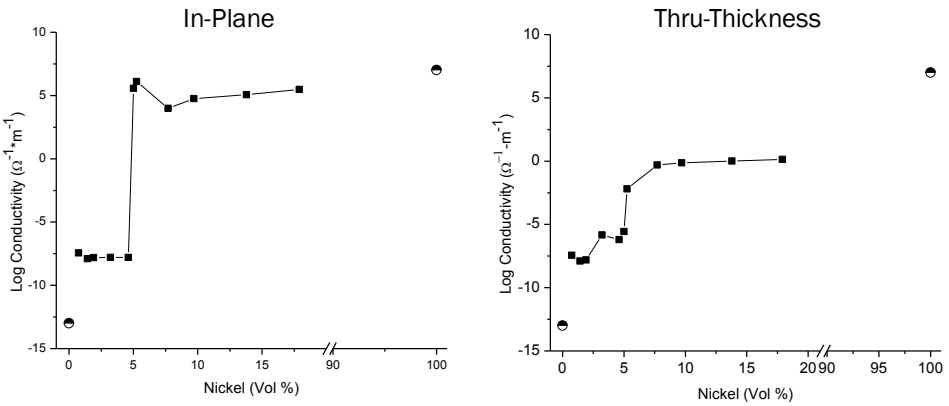

Figure 3-14: APS Conductivity of the sprayed composite vs. nickel content in the original blend. P_C occurs at 1.73 and 2.0 vol% Ni for In-plane and Thru thickness respectively.

Conductivity in HVOF composites also exhibits a clear P_C at 6.93 vol%Ni. Anisotropy in this system is not so accentuated. What appears as an interesting point is that the value for P_C is higher than in the APS system (6.93 and 5.25 vol%Ni respectively) which was not expected since the HVOF particle velocities was much higher and the flattening ratio as well.

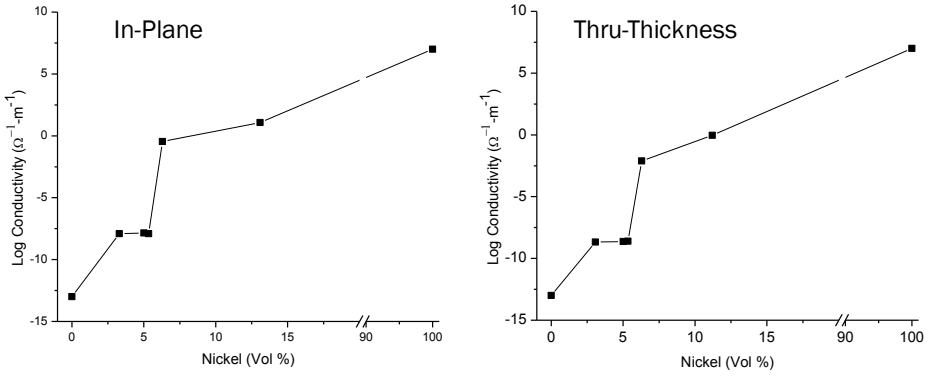

Figure 3-15 Conductivity of the HVOF sprayed composite as a function of nickel content in the original blend

3.3.3 Flattening ratio

Particle velocity and molten state greatly influences the flattening ratio. Experimental evidence has shown that different processes produce different

splat sizes and morphologies, Figure 3-8 shows that a typical wire-arc splat diameter is twice the diameter of an APS splat [56].

Figure 3-16 shows a field of alumina and nickel splats collected on polished and preheated stainless steel, nickel and alumina splats can be appreciated together in an optical micrograph and a 3D model of the splats using a Zygo white light interferometer system (Zygo Corp. Middlefield, CT, USA).

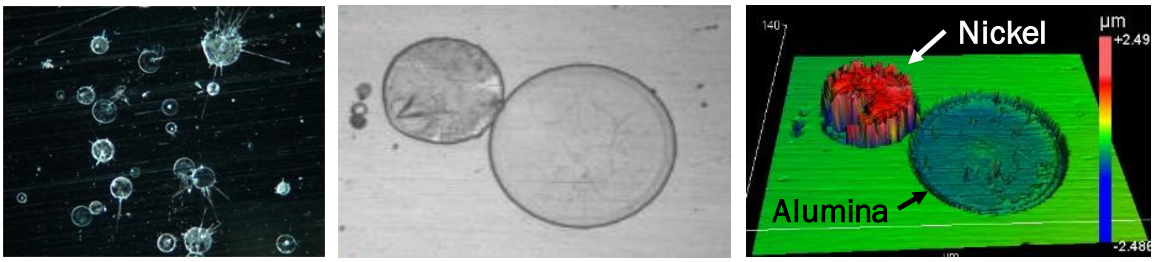

Figure 3-16: Collected splats of alumina and nickel over a polished stainless steel preheated substrate (left), Optical micrograph of alumina and nickel splats (center), 3-D model of the same image created using a Zygo white light interferometer system (right).

Resulting alumina splats were translucent in both composite compositions selected as well as with the two spray systems used, the substrate beneath the splat could be observed under the optical microscope with only a few visible defects (microcracks). Meanwhile, nickel splats were found to have a rough surface and in some cases were fragmented and in most cases contain a central hole. Two possible explanations are postulated to account for the incidence of such holes. One is due to the bounce-off of the solid core of a partially molten particle. The second is attributed to gas or moisture entrapment at the splat-substrate interface [4].

Li [57] stated that HVOF alumina smaller particle size (5-22 μm being a common range) and larger impact velocities (around 690 m/s) produces thin splats in the ~200–300 nm range that suggests the HVOF process can provide solidification kinetics with higher cooling rates (as compared to APS) and therefore a propensity to promote non-crystalline alumina, which would be

translucent and devoid cracks. It has been demonstrated that not only alumina but also YSZ splats can be translucent [58] since single crystals of oxide are transparent and become opaque because of grain boundaries, cracks and so on. However, if there are no cracks and if grain sizes are smaller than the wavelength of light, it can be translucent, because light cannot see what is smaller than its wavelength. Therefore, not only amorphous alumina but also nanocrystalline alumina can be transparent. [59] shows a field of alumina and nickel splats collected on stainless steel, Figure 3-16 shows and alumina splat translucent to the light under the Zygo and the crater beneath is reveled.

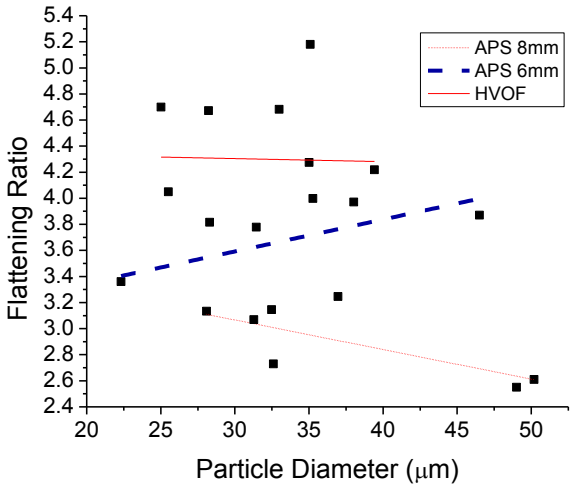

Figure 3-17 Flattening ratio vs. molten particle diameter for APS 6, 8mm and HVOF

The influence of particle size on flattening ratio is plotted in Figure 3-17 Flattening ratio vs. molten particle diameter for APS 6, 8mm and HVOF for HVOF, APS 6mm and 8mm nozzle. HVOF having higher particle velocity (~600 m/s) is expected to have higher flattening ratio than APS with particle velocities in the order of 350 and 170 m/s for 6 and 8mm nozzle respectively. Let's focus on the change in trend that is introduced with the change in nozzle diameter for the APS case: Molten state and particle velocity within each case is to be considered. Not all the particles impact the substrate at the same speed and at the same molten state; smaller particles will achieve faster velocities and larger ones may remain semi-molten in its core, at the same time the two configurations

in question provide very different average particle velocities adding to the difficulties in the interpretation of the problem.

3.3.4 Model approximation to percolation threshold

Comparing the results of flattening ratio and percolation threshold (P_C) obtained experimentally with the model developed by Liang [40] shown in Figure 3-5, its evident that the model underestimates the metal content needed to achieve P_C in the system and with the processes used. Table 3-9, Figure 3-18 and Figure 3-19 compile the experimental results and incorporate the values predicted by the model.

Table 3-9 Percolation threshold and flattening ratio for APS and HVOF composites

Process	Flattening ratio	Percolation Experimental (Vol%Ni)	Percolation Model (Vol%Ni)
HVOF	4.30	6.93	1.70
APS-6mm	3.75	5.25	2.00
APS-8mm	2.90	-	-

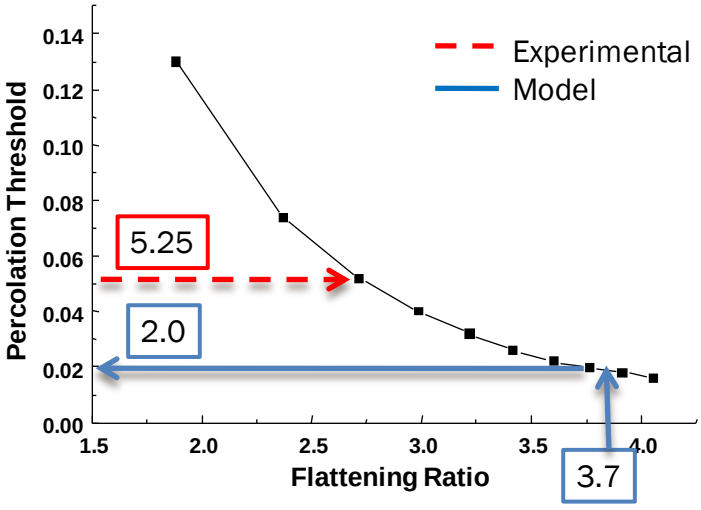

Figure 3-18: Percolation threshold for APS sprayed Al_2O_3-Ni

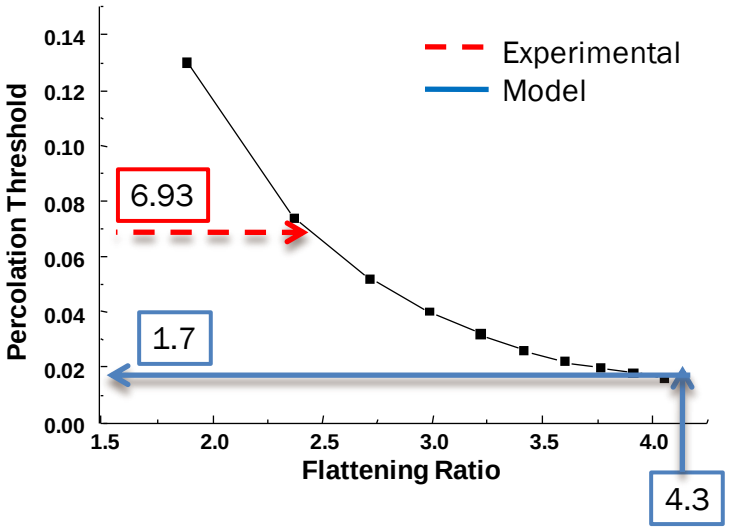

Figure 3-19: Percolation threshold for HVOF sprayed Al_2O_3-Ni

The difference between model and experimental results can be attributed to different sources: When splats are collected on a polished substrate the flattening ratio appears to be larger than in the actual coating The main reason behind this theory would be the higher roughness (> 5 Ra) for coatings vs. the usually very smooth surface (Ra<0.5) for polished stainless steel. Therefore,

- Actual flattening ratio should be smaller moving the curve towards higher percolation threshold.
- The model does not consider fragmentation nor splashing of particles upon impact. These phenomena would scatter the metallic phase into smaller more isolated particles, therefore moving the curve towards higher percolation threshold as is observed here.

3.4 Summary and conclusions

Percolation threshold (P_C) of thermal sprayed two component nickel-alumina composite was achieved at 5.25 and 6.93 vol%Ni for APS and HVOF respectively. The experimental results do not agree with the analytical model that correlates flattening ratio (F_R) with P_C. The model against which the comparison was made considered the splats as single units without taking into consideration splashing and inhomogeneities of the splat ‘s surface e.g., central hoe due to bounce-back of unmolten center core.

Experimental findings shows that the flattening ratio is affected by the roughness of the surface upon where particles impact; the smoother the surface the larger splat diameters are.

The deposition efficiency of the metallic component is higher than the ceramic resulting in a higher than nominal metal content in the thermal sprayed composite resistor.

REFERENCES

1. Omega, *The Pressure Strain and Force Handbook*. 8th ed. Vol. 3. 2008.
2. Fasching, M., F. Prinz, and L.E. Weiss, *"Smart" coatings: A technical note.* Journal of Thermal Spray Technology, 1995. **4**(2): p. 133-136.
3. Gutleber, J., et al. *Embedded Temperature and Heat Flux Sensors for Advanced Health monitoring of Turbine Engine components*. in *IEEE Aerospace Conference* 2006. Big Sky Montana.
4. Valarezo, A., et al. *Process Maps of Ni-Cr Coatings by HVOF Spraying*. in *Thermal spray Conference ITSC 2007*. 2007. Beijin, China: ASM International.
5. Longtin, J., et al. ***Direct-Write Thermal Spray for Embedded Sensor: Manufacturing and Integration onto Structures and Components***. in *NSF CMMI Research and Inovation Conference* 2009. Hawaii.
6. Clyne, T. and S. Gill, *Residual Stresses in Thermal Spray Coatings and Their Effect on Interfacial Adhesion: A Review of Recent Work.* Journal of Thermal Spray Technology, 1996. **5**(4): p. 401-418.
7. Li, W.-Y., C.-J. Li, and H. Liao, *Effect of annealing treatment on the microstructure and properties of cold-sprayed Cu coating.* Journal of Thermal Spray Technology, 2006. **15**(2): p. 206-211.
8. Matejicek, J. and S. Sampath, *In situ measurement of residual stresses and elastic moduli in thermal sprayed coatings: Part 1: apparatus and analysis.* Acta Materialia, 2003. **51**(3): p. 863-872.
9. Kuroda, S., T. Fukushima, and S. Kitahara, *Simultaneous measurement of coating thickness and deposition stress during thermal spraying.* Thin Solid Films, 1988. **164**: p. 157-163.
10. Kuroda, S. and T.W. Clyne, *The quenching stress in thermally sprayed coatings.* Thin Solid Films, 1991. **200**(1): p. 49-66.
11. Kobayashi, M., T. Matsui, and Y. Murakami, *Mechanism of creation of compressive residual stress by shot peening.* International Journal of Fatigue, 1998. **20**(5): p. 351-357.
12. Sampath, S., et al., *Development of process maps for plasma spray: case study for molybdenum.* Materials Science and Engineering A, 2003. **348**(1-2): p. 54-66.
13. Granet, I., *Strength of Materials*. Second ed. 1980: Reston.
14. Kuczynski, G.C., *Effect of Elastic Strain on the Electrical Resistance of Metals.* Physical Review, 1954. **94**(1): p. 61.
15. Polizzotto, C., *An extended shakedown theory for elastic-plastic-damage material models.* European journal of mechanichs, 1996. **15**(5): p. 825.
16. Sidhu, T.S., S. Prakash, and R.D. Agrawal, *Hot corrosion performance of a NiCr coated Ni-based alloy.* Scripta Materialia, 2006. **55**(2): p. 179-182.
17. Sidhu, T.S., S. Prakash, and R.D. Agrawal, *Characterisation of NiCr wire coatings on Ni- and Fe-based superalloys by the HVOF process.* Surface and Coatings Technology, 2006. **200**(18-19): p. 5542-5549.

18. Kuroda, S., T. Dendo, and S. Kitahara, *Quenching stress in plasma sprayed coatings and its correlation with the deposit microstructure.* Journal of Thermal Spray Technology, 1995. **4**(1): p. 75-84.
19. Sharma, A., R.J. Gambino, and S. Sampath. *Electrical Conduction in Thermally Sprayed Thin Metallic Coatings*. in *Mater. Res. Soc. Symp.* . 2006: MRS.
20. Zhu, D., et al., *Thermal conductivity of EB-PVD thermal barrier coatings evaluated by a steady-state laser heat flux technique.* Surface and Coatings Technology, 2001. **138**(1): p. 1-8.
21. Kerr, C. and P. Ivey, *An Overview of the Measurement Errors Associated wit Gas Turbine Aeroengine Pyrometer Systems.* Meas. Sci. Technol, 2002. **13**: p. 873-881.
22. Longtin, J., et al., *Sensors for harsh environments by direct-write thermal spray.* Sensors Journal, IEEE, 2004. **4**(1): p. 118-121.
23. Gambino, R.J.S.B., NY, US), Longtin, Jon Patrick (Port Jefferson, NY, US), Brogan, Jeffrey A. (Stony Brook, NY, US), Gutleber, Jonathan S. (Hungtinton, NY, US), Greenlaw, Robert J. (Hungtinton Beach, CA, US), *Thermocouples*. 2007: United States.
24. Chen, Q., et al., *Novel Sensor Fabrication Using Direct-Write Thermal Spray and Precision Laser Micromachining.* Journal of Manufacturing Science and Engineering, 2004. **126**(4): p. 830-836.
25. Gentleman, M.M. and D.R. Clarke, *Luminescence sensing of temperature in pyrochlore zirconate materials for thermal barrier coatings.* Surface and Coatings Technology, 2005. **200**(5-6): p. 1264-1269.
26. Bradley Iii, L.C., *A Temperature-Sensitive Phosphor Used to Measure Surface Temperatures in Aerodynamics.* Review of Scientific Instruments, 1953. **24**(3): p. 219-220.
27. Wickersheim, K., *Optical Temperature MEasurement Technique Utilizing Phosphors*. 1978: USA.
28. Clarke, D.R., *Embedded Optical Sensors for Thermal Barrier Coatings*. 2007, University of California, Santa Barbara.
29. Sellers, R., et al. *The use of optical pyrometers in axial flow turbines*. in *ASME, SAE and ASEE, Joint Propulsion Conference*. 1989. Monterrey, CA, USA.
30. Rowe, D.M., ed. *CRC Handbook of Thermoelectrics*. 1995, New York: CRC Press.
31. Lei, J. and L. Martin. *Advances in thin film sensor technologies for engine applications*. in *Turbo Expo*. 1997. Orlando, Florida, USA.
32. Lei, J.-F. and H.A. Will, *Thin-film thermocouples and strain-gauge technologies for engine applications.* Sensors and Actuators A: Physical, 1998. **65**(2-3): p. 187-193.
33. Hongseok, C., et al., *Microfabrication and characterization of metal-embedded thin-film thermomechanical microsensors for applications in hostile manufacturing environments.* Microelectromechanical Systems, Journal of, 2006. **15**(2): p. 322-329.

34. Pawlowski, L. and P. Fauchais, *Thermal Transport Properties of Thermally Sprayed Coatings.* Internationals Materials Reviews, 1992. **37**(6): p. 271-289.
35. Dutton, R., et al., *Effect of heat treatment on the thermal conductivity of plasma-sprayed thermal barrier coatings.* Journal of Thermal Spray Technology, 2000. **9**(2): p. 204-209.
36. Scott, J.F., *Applications of Modern Ferroelectrics.* Science, 2007. **315**(5814): p. 954-959.
37. Chien, C.L., *Magnetism and Giant Magneto-Transport Properties in Granular Solids.* Annual Review of Materials Science, 1995. **25**(1): p. 129-160.
38. Beach, G.S.D. and A.E. Berkowitz, *Co-Fe metal/native-oxide multilayers: a new direction in soft magnetic thin film design II. Microscopic characteristics and interactions.* Magnetics, IEEE Transactions on, 2005. **41**(6): p. 2053-2063.
39. Yamamoto, S., et al., *Fabrication of high-permeability ferrite by spark-plasma-sintering method.* Journal of Magnetism and Magnetic Materials, 2001. **235**(1-3): p. 218-222.
40. Liang, S., *Plasma Sprayed magnetic Composites: Process, Microstructure and Properties*, in *Materials Science and Engineering*. 2008, Stony Brook University: Stony Brook.
41. Michels, D., J. Hadeler, and V. Lienhard, *High-Heat Flux Heaters From VPS and HVOF Thermal SPray.* Experimental Heat Trnsfer, 1998. **11**(4): p. 341-359.
42. Liang, X.-G. and X. Ji, *Thermal conductance of randomly oriented composites of thin layers.* International Journal of Heat and Mass Transfer, 2000. **43**(19): p. 3633-3640.
43. Barthel, K., S. Rambert, and S. Siegmann, *Microstructure and polarization resistance of thermally sprayed composite cathodes for solid oxide fuel cell use.* Journal of Thermal Spray Technology, 2000. **9**(3): p. 343-347.
44. Newnham, R.E., *Composite electroceramics.* Ferroelectrics, 1986. **68**(1): p. 1 - 32.
45. Sharma, A., R.J. Gambino, and S. Sampath, *Anisotropic electrical properties in thermal spray metallic coatings.* Acta Materialia, 2006. **54**(1): p. 59-65.
46. Frisch, H.L. and M. Hammerseley, *Percolation processes and related topics.* Journal of the society for industrial and applied mathematics, 1963. **11**(4): p. 894.
47. Stauffer, D. and A. Aharony, *Introduction to Percolation Theory*. 2005.
48. Shafiro, B. and M. Kachanov, *Anisotropic effective conductivity of materials with nonrandomly oriented inclusions of diverse ellipsoidal shapes.* Journal of Applied Physics, 2000. **87**(12): p. 8561-8569.
49. Herman, H., S. Sampath, and R. McCune, *Thermal spray: Current status and future trends.* MRS Bulletin, 2000(Jluy 2000): p. 17-25.
50. Sampath, S., et al., *Direct-write thermal spraying of multilayer electronics and sensor structures*, in *Direct-write Technologies for Rapid Prototyping*

Applications, A. Pique and D. Chrisey, Editors. 2002, Academic Press. p. 261-302.
51. Finot, M., et al., *Curvature changes during thermal cycling of a compositionally graded Ni---Al2O3 multi-layered material.* Materials Science and Engineering A, 1996. **205**(1-2): p. 59-71.
52. Hasan, M., et al., *Effect of spray parameters on residual stress build-up of HVOF sprayed aluminium/tool-steel functionally graded coatings.* Surface and Coatings Technology, 2008. **202**(16): p. 4006-4010.
53. Wan, Y.P., et al., *An advanced model for plasma spraying of functionally graded materials.* Journal of Materials Processing Technology, 2003. **137**(1-3): p. 110-116.
54. Khor, K.A., Z.L. Dong, and Y.W. Gu, *Plasma sprayed functionally graded thermal barrier coatings.* Materials Letters, 1999. **38**(6): p. 437-444.
55. Kesler, O., et al., *Determination of processing-induced stresses and properties of layered and graded coatings: Experimental method and results for plasma-sprayed Ni---Al2O3.* Acta Materialia, 1997. **45**(8): p. 3123-3134.
56. Sampath, S., et al., *Role of thermal spray processing method on the microstructure, residual stress and properties of coatings: an integrated study for Ni-5 wt.%Al bond coats.* Materials Science and Engineering A, 2004. **364**(1-2): p. 216-231.
57. Li, L., et al., *Suppression of crystallization during high velocity impact quenching of alumina droplets: Observations and characterization.* Materials Science and Engineering: A, 2007. **456**(1-2): p. 35-42.
58. Kulkarni, A., et al., *Studies of the microstructure and properties of dense ceramic coatings produced by high-velocity oxygen-fuel combustion spraying.* Materials Science and Engineering A, 2004. **369**(1-2): p. 124-137.
59. Gentleman, M.M. and D.R. Clarke, *Concepts for luminescence sensing of thermal barrier coatings.* Surface and Coatings Technology. **188-189**: p. 93-100.